# Superconductivity and magnetic and transport properties of single-crystalline $CaK(Fe_{1-x}Cr_x)_4As_4$

M. Xu, J. Schmidt, M. A. Tanatar, R. Prozorov, S. L. Bud'ko, and P. C. Canfield*
*Ames National Laboratory, Iowa State University, Ames, Iowa 50011, USA*
*and Department of Physics and Astronomy, Iowa State University, Ames, Iowa 50011, USA*

(Received 9 February 2023; revised 21 March 2023; accepted 31 March 2023; published 12 April 2023)

Members of the $CaK(Fe_{1-x}Cr_x)_4As_4$ series have been synthesized by high-temperature solution growth in single-crystalline form and characterized by x-ray diffraction, elemental analysis, and magnetic and transport measurements. The effects of Cr substitution on the superconducting and magnetic ground states of $CaKFe_4As_4$ ($T_c = 35$ K) have been studied. These measurements show that the superconducting transition temperature decreases monotonically and is finally suppressed below 1.8 K as $x$ is increased from 0 to 0.038. For $x$-values greater than 0.012, signatures of a magnetic transition can be detected in magnetic measurements with the associated features in the transport measurements becoming detectable for $x \geqslant 0.038$. The magnetic transition temperature increases in a roughly linear manner as Cr substitution increases. A temperature-composition ($T$-$x$) phase diagram is constructed, revealing a half-dome of superconductivity with the magnetic transition temperature, $T^*$, appearing near 22 K for $x \sim 0.017$ and rising slowly up to 60 K for $x \sim 0.077$. The $T$-$x$ phase diagrams for $CaK(Fe_{1-x}T_x)_4As_4$ for $T =$ Cr and Mn are essentially the same despite the nominally different band filling; this is in marked contrast to $T =$ Co and Ni series for which the $T$-$x$ diagrams scale by a factor of 2, consistent with the different changes in band filling Co and Ni would produce when replacing Fe. Superconductivity of $CaK(Fe_{1-x}Cr_x)_4As_4$ is also studied as a function of magnetic field. A clear change in $H'_{c2}(T)/T_c$, where $H'_{c2}(T)$ is $dH_{c2}(T)/dT$, at $x \sim 0.012$ is observed and probably is related to a change of the Fermi surface due to magnetic order. Coherence length and the London penetration depths are also calculated based on $H_{c1}$ and $H_{c2}$ data. Both of them as a function of $x$ show changes near $x = 0.012$, again consistent with Fermi surface changes associated with the magnetic ordering seen for higher $x$-values.

DOI: 10.1103/PhysRevB.107.134511

## I. INTRODUCTION

The study of Fe-based superconductors has led to extensive experimental interest, and their variety offers the opportunity to understand unconventional superconductivity in a broader sense. Fe-based superconductor families share similar crystal structures [1–12] and phase diagrams [13–21], which suggests a relationship between, or proximity of, superconducting and magnetic and/or nematic ordering or fluctuations. These relationships between superconductivity and magnetic as well as structural transitions and fluctuations are believed to be key to understanding unconventional superconductivity [22].

Though Fe-based superconductors have a moderate degree of structural diversity, three main structural classes—$AeFe_2As_2$ ($Ae =$ alkaline earth) (122) families [2–4,13–17], $AeAFe_4As_4$ ($A =$ alkaline metal) (1144) family [5–7,9,10,18], and FeSe [8,19]—provide a microcosm of many key questions at hand. Compared with the interplay between stripelike antiferromagnetic order, nematicity, and superconductivity in the doped 122-systems at ambient pressure [3,16], the electron-doped $CaK(Fe_{1-x}T_x)_4As_4$, $T =$ Ni and Co system has hedgehog-spin-vortex-crystal (h-SVC) type antiferromagnetic (AFM) order and superconductivity interacting with each other without any structural phase transition [18,23].

Substitutions on $Ae$ and $A$ sites [24] suggest that $T_c$ is linked to a structural distortion, in particular to the $c/a$ ratio. Substitution on the transition-metal site, however, tells a different story. On the one hand, the structural relation on $T_c$ of substituted $CaKFe_4As_4$ has been studied. The phase diagrams of Co and Ni substitutions of $CaKFe_4As_4$ scaled almost exactly as a function of band-filling change, so the comparison between $CaKFe_4As_4$ and $Ba_{0.5}K_{0.5}Fe_2As_2$ based on their similar, nominal electron counts seems justified. One the other hand, given that $CaK(Fe_{1-x}T_x)_4As_4$ allows for the study of how nominal hole-doping with Mn and Cr can affect the superconducting and magnetic properties of this system, it is very important to see how their $T$-$x$ phase diagrams compare with each other as well as those for $T =$ Co and Ni.

We have recently found that for $CaK(Fe_{1-x}T_x)_4As_4$, $T =$ Mn, Mn is a far more local-moment-like impurity than $T =$ Co or Ni are. We also found that the substitution level of $CaK(Fe_{1-x}Mn_x)_4As_4$ can only go to up to $x = 0.036$. Beyond that level, 1144 phase is not stabilized with the similar synthesis condition. This limited the exploration of the hole-doped 1144 phase diagram and the evolution of the h-SVC-type antiferromagnetic transition. Cr offers twice the amount of nominal hole-doping per $x$ and, like Mn, it can sometimes manifest local-moment-like properties in intermetallic samples. As such, Cr substitution offers a great of opportunity to further our understanding of the behavior of h-SVC-type antiferromagnetism in the 1144 system.

*canfield@ameslab.gov

 

In this paper, we detail the synthesis and characterization of $CaK(Fe_{1-x}Cr_x)_4As_4$ single crystals. A temperature-composition ($T$-$x$) phase diagram is constructed by elemental analysis and magnetic and transport measurements. In addition to creating the $T$-$x$ phase diagram, coherence lengths and the London penetration depths are also calculated based on $H_{c1}$ and $H_{c2}$ data obtained from measurements. The data for Cr-substituted 1144 are added on the $\lambda^{-2}$ versus $\sigma\ T_c^2$ plot and compared with the Mn substitution. Finally, for the temperature versus change of electron count, $|\Delta e^-|$, the phase diagram for $CaK(Fe_{1-x}T_x)_4As_4$ single crystals, $T$ = Cr, Mn, Ni, and Co, is also presented and discussed. By comparing all four $T$ = Cr, Mn, Ni, and Co substitutions, we find that whereas for $T$ = Ni and Co $CaK(Fe_{1-x}T_x)_4As_4$ the temperature-substitution phase diagrams scale with additional electrons [in much the same way that the $Ba(Fe_{1-x}TM_x)_2As_2$ phase diagrams do for $T$ = Ni and Co], for $T$ = Cr and Mn the temperature substitution phase diagrams are essentially identical when plotted more simply as $T$-$x$ diagrams, suggesting that for Cr and Mn there may be other variables or mechanisms at play.

## II. CRYSTAL GROWTH AND EXPERIMENTAL METHOD

Single-crystalline $CaK(Fe_{1-x}Cr_x)_4As_4$ samples were grown by high-temperature solution growth [25] out of FeAs flux in the manner similar to $CaK(Fe_{1-x}Mn_x)_4As_4$ [21]. Lumps of potassium metal (Alfa Aesar 99.95%), distilled calcium metal pieces [Ames Laboratory, Materials Preparation Center (MPC 99.9%)], and $Fe_{0.512}As_{0.488}$ and $Cr_{0.512}As_{0.488}$ precursor powders were loaded into a 1.7 mL fritted alumina Canfield Crucible Set [26] (LSP Industrial Ceramics, Inc.) in an argon-filled glove-box. The ratio of K:Ca:$Fe_{0.512}As_{0.488}$ and $Cr_{0.512}As_{0.488}$ was 1.2:0.8:20. A 1.3 cm outer diameter and 6.4-cm-long tantalum tube which was used to protect the silica ampoule from reactive vapors was welded with the crucible set in a partial argon atmosphere inside. The sealed Ta tube was then sealed into a silica ampoule, and the ampoule was placed inside a box furnace. The furnace was held for 2 h at 650 °C before increasing to 1180 °C and held there for 5 h to make sure the precursor was fully melted. The furnace was then fast cooled from 1180 to 980 °C in 1.5 h. Crystals were grown during a slow cool-down from 980 to 915 °C over 100–150 h dependent on substitution level. After 1–2 h at 915 °C, the ampoule was inverted into a centrifuge and spun to separate the remaining liquid from the grown crystals. Metallic, platelike crystals were obtained. The average size and thickness decreased by a factor 2–4 as $x$ is increased. The largest crystal is about a centimeter size, as shown in Fig. 1.

Single crystals of $CaK(Fe_{1-x}Cr_x)_4As_4$ are soft and malleable as $CaKFe_4As_4$ and are difficult to grind for powder x-ray diffraction measurements. Diffraction measurements were carried out on single-crystal samples, which were cleaved along the (001) plane, using a Rigaku MiniFlex II powder diffractometer in Bragg-Brentano geometry with Cu $K\alpha$ radiation ($\lambda$ = 1.5406 Å) [27].

The Cr substitution levels ($x$) of the $CaK(Fe_{1-x}Cr_x)_4As_4$ crystals were determined by energy-dispersive spectroscopy (EDS) quantitative chemical analysis using an EDS detector (Thermo NORAN Microanalysis System, model C10001) attached to a JEOL scanning-electron microscope. The compositions of platelike crystals were measured at three separate positions on each crystal's face (parallel to the crystallographic $ab$-plane) after cleaving them. An acceleration voltage of 16 kV, a working distance of 10 mm, and a take-off angle of 35° were used for measuring all standards and crystals with unknown composition. Pure $CaKFe_4As_4$ was used as a standard for Ca, K, Fe, and As quantification. $LaCrGe_3$ and $YCr_6Ge_6$ were used as standards for Cr, both leading to consistent results without a significant difference within the experimental error (~0.001). The spectra were fitted using NIST-DTSA II Microscopium 2020-06-26 software [28]. Different measurements on the same sample reveal good homogeneity in each crystal, and the average compositions and error bars were obtained from these data, accounting for both inhomogeneity and goodness of fit of each spectra.

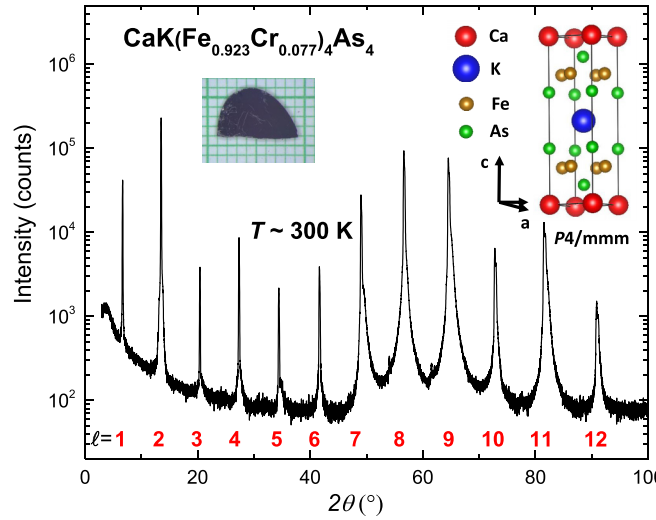


FIG. 1. X-ray diffraction data of $CaK(Fe_{0.923}Cr_{0.077})_4As_4$ showing ($00l$) diffraction peaks from in-house diffraction measurements on a single-crystalline plate plotted on a semilog scale. The value of $l$ is shown in red under each peak. The left inset shows the picture of $CaK(Fe_{0.988}Cr_{0.012})_4As_4$ single crystal over a millimeter grid paper. The right inset shows crystal structure of $CaKFe_4As_4$. Note that $l$ = odd ($00l$) lines are evidence of the ordered $CaKFe_4As_4$ structure [5,6].

Temperature- and magnetic-field-dependent magnetization and resistance measurements were carried out by using Quantum Design (QD), Magnetic Property Measurement Systems (MPMS and MPMS3), and Physical Property Measurement Systems (PPMS). Temperature- and magnetic-field-dependent magnetization measurements were taken for $H \| ab$ by placing the platelike sample between two collapsed plastic straws with the third, uncollapsed, straw providing support as a sheath on the outside or by use of a quartz sample holder. The single-crystal samples of $CaK(Fe_{1-x}Cr_x)_4As_4$ measured in the MPMS and MPMS3 have platelike morphology with length and width from 3 to 10 mm and thickness ($c$-axis) 50–200 μm. The approximate effective demagnetizing factor $N$ ranges from 0.007 to 0.077 with magnetic field applied parallel to the crystallographic $ab$ plane [29].

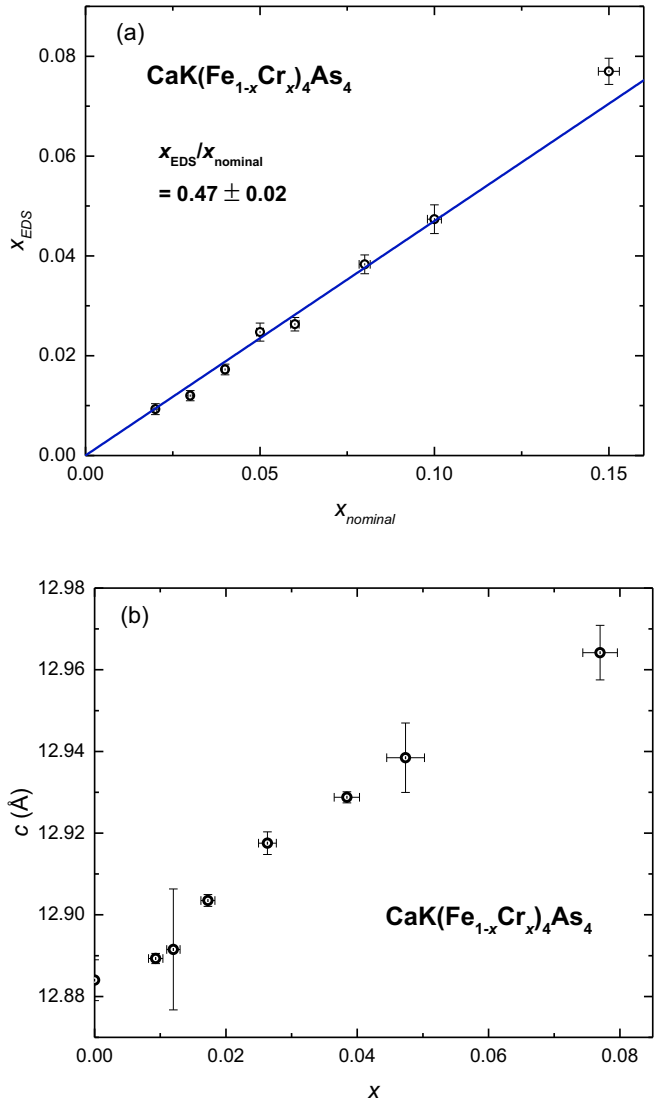


FIG. 2. (a) EDS measured Cr concentration vs nominal Cr concentration for the $CaK(Fe_{1-x}Cr_x)_4As_4$ series. The line is the linear fit of the data with fixed intercept to 0. (b) Plot of $c$ lattice parameters as a function of substitution level $x$. $c$ lattice parameters are calculated by the single-crystalline plate x-ray diffraction plot [27].

AC electrical resistance measurements were performed in a standard four-contact geometry using the ACT option of the PPMS, with a 3 mA excitation and a frequency of 17 Hz. 50-μm-diam Pt wires were bonded to the samples with silver paint (DuPont 4929N) with contact resistance values of about 2–3 Ω. The magnetic field, up to 90 kOe, was applied along $c$ or $ab$ directions, perpendicular to the current, with the current flowing in the $ab$ plane in both cases.

Contacts for interplane resistivity measurements were soldered using tin. The top and bottom surfaces of the samples were covered with Sn solder [30,31], and 50 μm silver wires were attached to enable measurements in a pseudo-four-probe configuration. Soldering produced contacts with resistance typically in the 10 μΩ range. Interplane resistivity was measured using a two-probe technique with currents in a 1–10 mA range (depending on sample resistance, which is typically 1 mΩ). A four-probe scheme was used down to the sample to measure series-connected sample, $R_s$, and contact, $R_c$, resistance. Taking into account that $R_s \gg R_c$, contact resistance represents a minor correction of the order of 1–5 %. The details of the measurement procedure can be found in Refs. [32–34]. The results of the measurements are in good agreement with similar measurements on pure $CaKFe_4As_4$ [6].

Measurements with current along the $c$-axis suffer strongly from interlayer connectivity due to the micaceous nature of single crystals. To ascertain reproducibility, we performed measurements of $\rho_c$ on two to five samples for each Cr concentration, and we obtained qualitatively similar temperature dependencies of the electrical resistivity, as represented by the ratio of resistivities at room and low temperatures, $\rho_c(0)/\rho_c(300)$. The resistivity $\rho_c(300\ \mathrm{K})$ was in the range 1–2 mΩ cm, corresponding to an anisotropy ratio $\rho_c/\rho_a \approx 3$–6 at 300 K.

## III. $CaK(Fe_{1-x}Cr_x)_4As_4$ STRUCTURE AND COMPOSITION

Figure 1 presents single-crystal diffraction data of $CaK(Fe_{1-x}Cr_x)_4As_4$ with $x_{\mathrm{EDS}} = 0.077$, which is the largest substitution level obtained. Attempts to grow crystals with $x_{\mathrm{EDS}} > 0.077$ failed to yield mm-sized or larger samples that could be identified as Cr-doped 1144. From the figure, we can see that all $(00l)$, $l \leqslant 12$, are detected. The $h + k + l =$ odd peaks which are forbidden for the $I4/mmm$ structure of the 122 phase [5] can be clearly found. This indicates that the sample has the anticipated $P4/mmm$ structure associated with the $CaKFe_4As_4$ structure [5,6,18].

The Cr substitution, $x_{\mathrm{EDS}}$, determined by EDS is shown in Fig. 2(a) for different crystals as a function of the nominal Cr fraction, $x_{\mathrm{nominal}}$, that was originally used for the growth. Error bars account for both possible inhomogeneity of substitution and goodness of fit of each EDS spectra. A clear correlation can be seen between the nominal and the measured substitution levels, with a proportionality factor of 0.47 ± 0.02. For comparison, the ratios of measured to nominal Mn, Ni, and Co fraction in the corresponding $CaK(Fe_{1-x}T_x)_4As_4$ are 0.60, 0.64, and 0.79, respectively [18,21]. From this point onward, when substitution level $x$ is referred to, it will be the EDS value of $x$. Figure 2(b) presents $c$ lattice parameters as a function of $x$. The $c$ lattice parameter increases monotonically as Cr substitution level increases, which is consistent with the larger radius of Cr as compared to Fe. $c$ lattice parameter values are calculated using the single-crystalline plate x-ray diffraction data taken in Bragg-Brentano geometry in a standard powder diffractometer [27]. In Mn-1144 $[CaK(Fe_{1-x}Mn_x)_4As_4]$ [21], the evolution of the $c$ lattice parameter was difficult to determine due to the small difference in radius between Fe and Mn and low substitution levels of Mn. The highest Mn substitution level $x$ was 0.036 in Mn-1144 as compared to 0.077 in Cr-1144.

## IV. DATA ANALYSIS AND PHASE DIAGRAM

Figure 3 shows the low-temperature (1.8–45 K), zero-field-cooled-warming (ZFCW) magnetization for $CaK(Fe_{1-x}Cr_x)_4As_4$ single crystals for $H_{||ab} = 50$ Oe [ZFCW

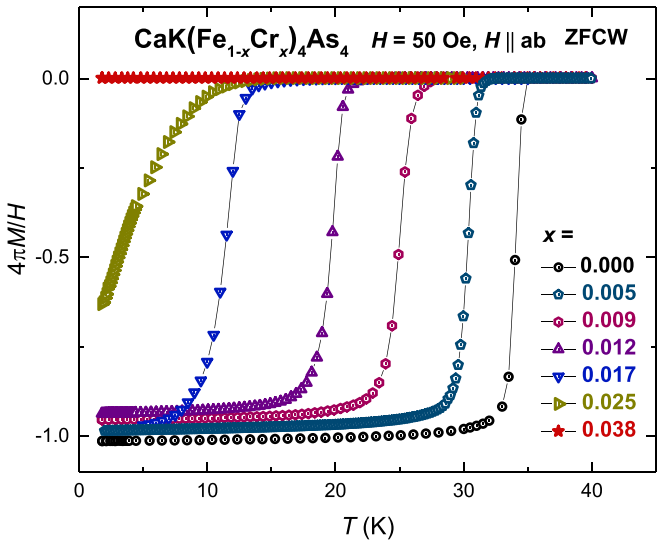


FIG. 3. Zero-field-cooled-warming (ZFCW) low-temperature magnetization as a function of temperature for $CaK(Fe_{1-x}Cr_x)_4As_4$ single crystals with a field of 50 Oe applied parallel to the crystallographic *ab* plane. $M$ is the volumetric magnetic moment with cgs unit emu $cm^{-3}$ or Oe.

magnetization and field-cooled (FC) data for an $x = 0.017$ sample can be found in Fig. 19 in the Appendix]. $M$ is the volumetric magnetization in this figure, and it is calculated by using the density of $CaKFe_4As_4$, which is determined to be 5.22 $g/cm^3$ from the lattice parameters at room temperature [5]. A magnetic field of 50 Oe was applied parallel to the *ab* plane (i.e., parallel to the surface of the platelike crystal). The superconducting transitions ($T_c$) are clearly seen in this graph except for the substitution value $x = 0.038$. As the value of the Cr substitution, $x$, increases, the superconducting

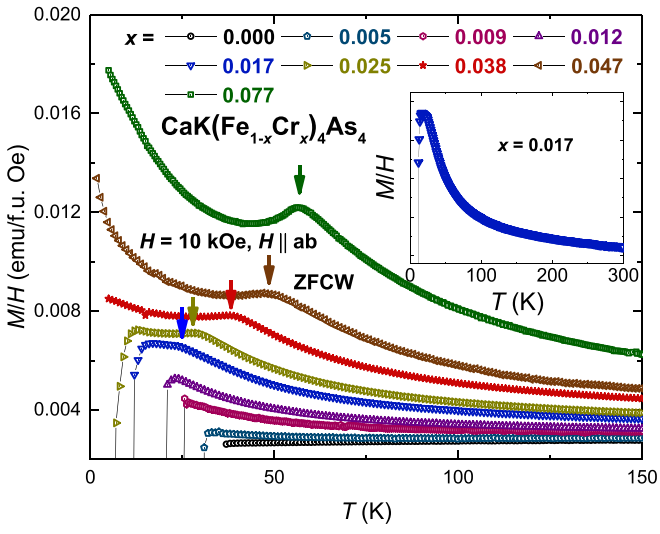


FIG. 4. Low-temperature magnetization divided by applied field as a function of temperature for $CaK(Fe_{1-x}Cr_x)_4As_4$ single crystals with a field of 10 kOe applied parallel to the crystallographic *ab* plane. The inset shows the $CaK(Fe_{0.983}Cr_{0.017})_4As_4$ single-crystal magnetization for $5 < T < 300$ K. Small vertical arrows indicate the location of $T^*$; see the Appendix for the criterion.

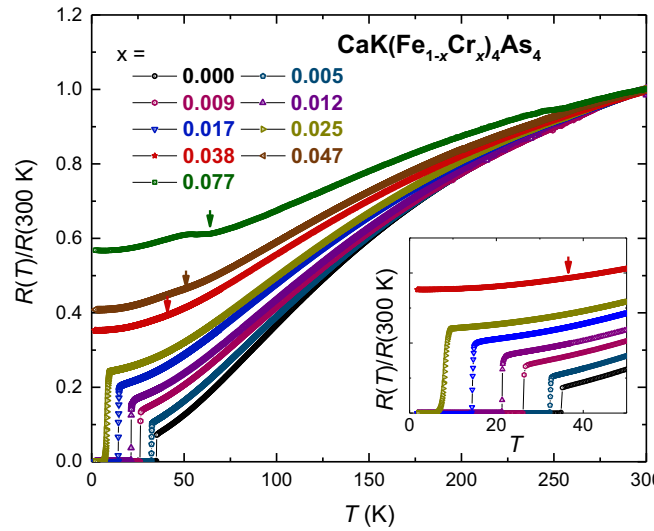


FIG. 5. Temperature dependence of normalized resistance, $R(T)/R(300\ \mathrm{K})$, of $CaK(Fe_{1-x}Cr_x)_4As_4$ single crystals showing the suppression of the superconducting transition $T_c$ and the appearance and evolution of a kinklike feature, marked with arrows. The criterion used to determine $T^*$ from this kink-feature is outlined and discussed in the Appendix.

transition temperature decreases. For $x = 0.025$, a full magnetic shielding is not reached by 1.8 K.

Figure 4 shows the low-temperature (5–150 K) $M(T)/H$ data for $CaK(Fe_{1-x}Cr_x)_4As_4$ single crystals with 10 kOe field applied parallel to the crystallographic *ab* plane. The appearance of first a Curie-Weiss tail and later a kinklike feature after adding Cr is similar to Mn substituted 1144. The inset shows $M(T)/H$ of a $CaK(Fe_{0.983}Cr_{0.017})_4As_4$ single crystal over a wider temperature range. As Cr is added, the Curie-tail-like feature grows. The $M(T)$ data above transitions can be fitted by a $C/(T + \theta) + \chi_0$ function as long as Cr doping levels are larger than 0.005 ($x > 0.005$). The effective moment versus $x$ data is shown in Fig. 18 in the Appendix; $\mu_{\mathrm{eff}}$ calculated per Cr is found to be ~4 $\mu$B. Kinklike features are found above 20 K for $x > 0.012$ at a temperature $T^*$, which very likely indicates an antiferromagnetic transition. Similar kinklike features were correlated with AFM order in $CaK(Fe_{1-x}Mn_x)_4As_4$ [21,35]. As $x$ increases from 0.017 to 0.077, the temperature $T^*$ increases from ~ 20 to ~ 60 K. The criterion for determining $T^*$ and more discussion about the Curie-tail are shown in the Appendix.

Figure 5 presents the temperature-dependent, normalized, electrical resistance of $CaK(Fe_{1-x}Cr_x)_4As_4$ single crystals. RRR (the ratio of 300 K and low-temperature resistance just above $T_c$) decreases as Cr substitution increases, which is consistent with the increase of disorder and/or the possible change of the density of states near the Fermi surface by band-filling. The superconducting transition temperatures decrease as Cr is added to the system. When $x = 0.038$, there is no signature of a superconducting transition detectable above 1.8 K. With increasing Cr content, a kink appears for $x > 0.025$ and rises to about 60 K for $x = 0.077$, and features become more clearly resolved with increasing substitution. A similar feature also appeared in Mn-, Ni-, and Co-substituted $CaKFe_4As_4$

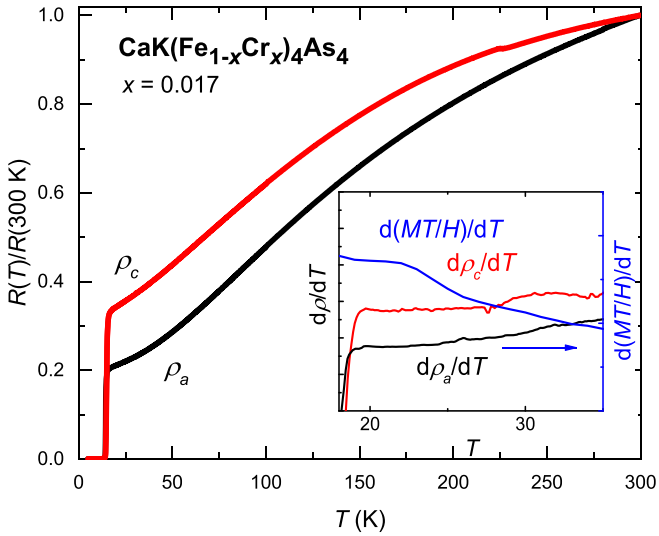


FIG. 6. Temperature dependence of normalized resistance, $R(T)/R(300\ \mathrm{K})$, of $CaK(Fe_{1-x}Cr_x)_4As_4$ single crystals with $x = 0.017$ for electrical currents along the $a$-axis (black) and along the $c$-axis (red). The inset shows resistivity derivatives plotted against $d(MT/H)/dT$ (blue). The onset of the feature in the $d(MT/H)/dT$ curve at ~25 K is accompanied by flattening in the $c$-axis resistivity derivative, but without a clear anomaly. No features are observed in the $d[R/R(300\ \mathrm{K})]/dT$ curve for in-plane current (black line in the inset).

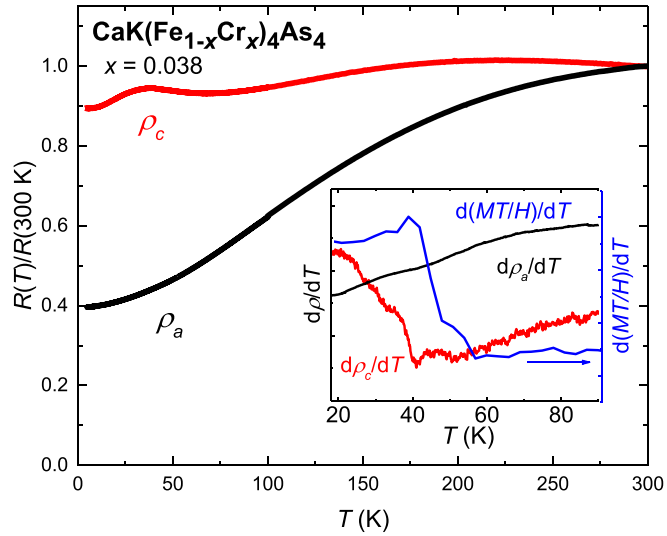


FIG. 7. Temperature dependence of normalized resistance, $R(T)/R(300\ \mathrm{K})$, of $CaK(Fe_{1-x}Cr_x)_4As_4$ single crystals with $x = 0.038$ for electrical currents along the $a$-axis (black) and along the $c$-axis (red). The inset shows resistivity derivatives plotted against $d(MT/H)/dT$ (blue, right axis). The peak in the $d(MT/H)/dT$ curve at ~ 42 K is accompanied by a clear feature in the $c$-axis resistivity derivative, but only with a very broad anomaly, if any, for the in-plane transport.

electrical resistance measurements [18,21]. The criterion for determining the transition temperature, $T^*$, associated with this kink is shown in the Appendix in Fig. 21(c), where $R(T)$ and $dR(T)/dT$ are both shown.

Figures 6 and 7 compare the normalized electrical resistivity of $CaK(Fe_{1-x}Cr_x)_4As_4$ single crystals for electrical currents along the $a$-axis in the tetragonal plane (black lines in the main panels) with those along the tetragonal $c$-axis (red curves in the main panels). Samples with $x = 0.017$, Fig. 6, are in the range of SC and AFM coexistence; samples with $x = 0.038$, Fig. 7, are in the range where superconductivity is suppressed (see Fig. 8, below). The interplane resistivity of the samples with $x = 0.017$ shows a broad crossover close to room temperature, above which the rate of resistivity increase with temperature gets notably slower, and a much milder feature is found in in-plane transport. This is very similar to the results on the parent compound $x = 0$ [6]. For samples with $x = 0.038$, Fig. 7, the interplane resistivity (red curve, main panel) reveals a clearly nonmonotonic dependence. The crossover transforms into a clear maximum above 200 K, followed by a second maximum centered at about 35 K, close to the temperature of long-range magnetic ordering.

Insets in the figures compare the derivatives of the normalized resistivities for two current directions with $d(MT/H)/dT$ (blue lines, right scale) [36]. For sample $x = 0.017$ in Fig. 6, no clear features are observed in the resistivity derivatives, however some flattening is observed for $c$-axis resistivity. For samples with $x = 0.038$, the peak in $d(MT/H)/dT$ at ~42 K is in good agreement with the feature in the derivative of interplane resistivity. A feature in the derivative of in-plane resistivity is notably less pronounced (black curve in the inset in Fig. 7).

In some cases, the features associated with magnetic ordering in the FeAs-based superconductors are clearer for current

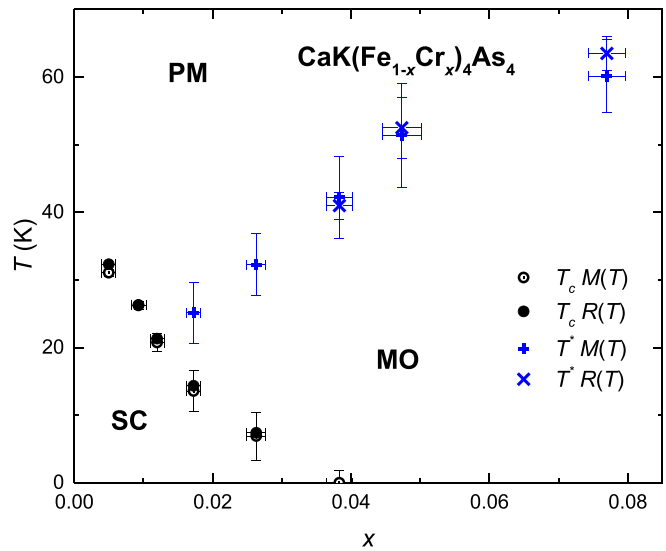


FIG. 8. Temperature-composition phase diagram of $CaK(Fe_{1-x}Cr_x)_4As_4$ single crystals as determined from resistance $[R(T)]$ and magnetization $[M(T)]$ measurements. The circular symbols denote the $T_c$ phase line, and the crosslike symbols denote the $T^*$ phase line, most likely associated with antiferromagnetic order. Superconducting (SC), magnetically ordered (MO), and paramagnetic (PM) regions are denoted. Details of how the MO line extends into the SC state are not addressed in this phase diagram.

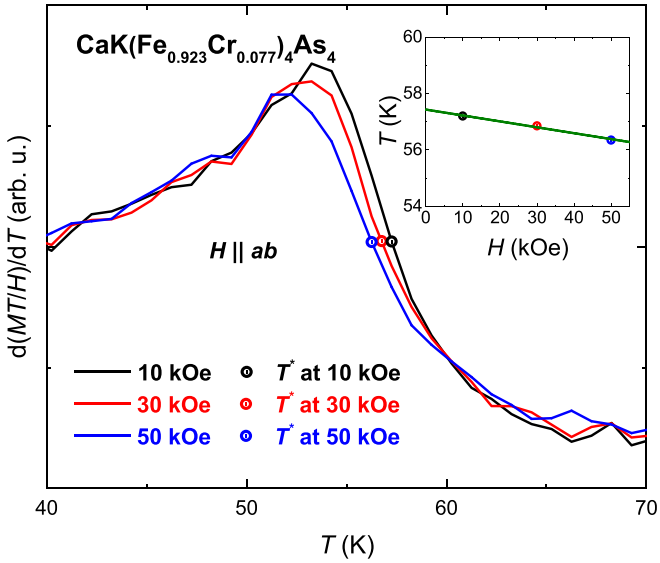


FIG. 9. $d(MT/H)/dT$ vs $T$ of $CaK(Fe_{0.923}Cr_{0.077})_4As_4$ single crystal with 10, 30, and 50 kOe applied parallel to the crystallographic *ab* plane. $T^*$ at different field are shown as points on the figure. The inset shows transition temperature, $T^*$, inferred for different applied field values using the same criterion shown in the Appendix. The solid green line is a linear fit to the data points, extrapolating to 54.7 K for $H = 0$.

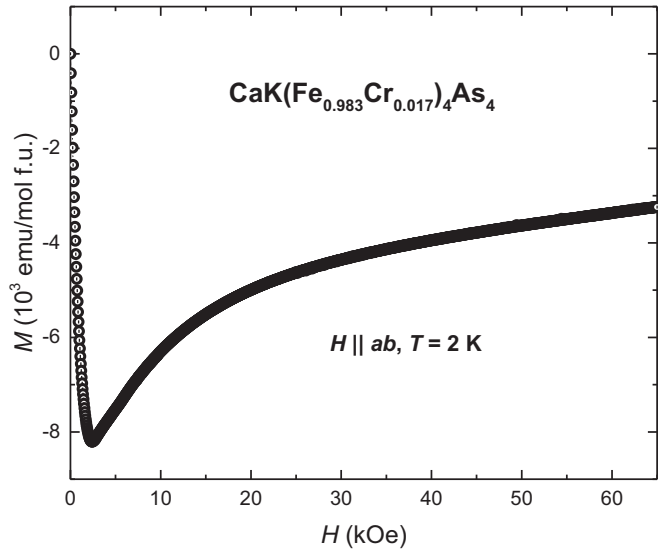


FIG. 10. Magnetization of a single crystal of $CaK(Fe_{0.983}Cr_{0.017})_4As_4$ as a function of magnetic field applied parallel to the crystallographic *ab* plane at 2 K, after zero applied field cooling (ZFC) to 2 K so as to have demagnetization done at 60 K before cooling minimizes the remnant magnetic field.

flow along the *c*-axis as opposed to current flow in the basal *ab*-plane. This is believed to be due to an alternating arrangement of the magnetic moments along the *c*-axis direction, providing partial gapping of the Fermi surface affecting interplane transport more strongly [34]. The clarity of features increases with $x$ in $CaK(Fe_{1-x}Cr_x)_4As_4$, making them clearly visible in the raw resistivity data for $x = 0.077$ (see the Appendix, Fig. 23).

Figure 8 summarizes the transition temperature results inferred from magnetization and resistance measurements, plots the superconducting and magnetic transitions as a function of substitution, and constructs the $T$-$x$ phase diagram for the $CaK(Fe_{1-x}Cr_x)_4As_4$ system. As depicted in this phase diagram, increasing Cr substitution (i) suppresses $T_c$ monotonically with it extrapolating to 0 K by $x \sim 0.03$, and (ii) stabilizes a new transition, presumably an antiferromagnetic one, for $x \gtrsim 0.017$ with the transition temperature rising from ~20 K for $x = 0.017$ to ~60 K for $x = 0.077$. Each phase line is made out of data points inferred from $R(T)$ and $M(T)$ measurements, illustrating the good agreement between our criteria for inferring $T_c$ and $T^*$ from magnetization and resistivity data. The $CaK(Fe_{1-x}T_x)_4As_4$ series, $T =$ Mn, Co, and Ni, have qualitatively similar phase diagrams, with the quantitative differences being associated with the substitution levels necessary to induce the magnetic phase and to suppress superconductivity. We were not able to infer the behavior of $T^*$ once it drops below $T_c$, but if it is similar to other $T$ substitution [35,37], $T^*$ should be suppressed very fast in the superconducting state. Further comparison of the $CaK(Fe_{1-x}Cr_x)_4As_4$ phase diagram to the phase diagrams of the $CaK(Fe_{1-x}T_x)_4As_4$ series will be made in the Discussion section below.

Given that the $R(T)$ data were taken in zero applied field whereas the $M/H(T)$ data shown in Fig. 4 were taken in 10 kOe, it is prudent to examine the field dependence of transition associated with $T^*$. In Fig. 9 we show the $d(MT/H)/dT$ data [36] for the $x = 0.077$ sample for $H||ab = 10$, 30, and 50 kOe. As is commonly seen for an antiferromagnetic phase transition, increasing a magnetic field leads to a monotonic suppression of $T^*$. The inset to Fig. 9 shows that the extrapolated, $H = 0$, $T^*$ value would be 57.4 K as compared to the value of 57.2 K for 10 kOe. This further confirms that there should be (and there actually is) good agreement between the $T^*$ values inferred from 10 kOe magnetization data and the $T^*$ values inferred from the resistance data in Fig. 8. In addition, these data suggest that magnetic field could be used to fine-tune the value of $T^*$, if needed.

## V. SUPERCONDUCTING CRITICAL FIELDS AND ANISOTROPY

Superconductivity can be studied as a function of field (in addition to temperature and doping). Before we present our $H_{c2}(T)$ results, based on $R(T, H)$ data, it is useful to check the $M(H)$ data. We start with $M(H)$ data for $x = 0.017$, $T_c =$ 14.4 K, taken over a wide field range. The 2 K $M(H)$ data shown in Fig. 10 are classically nonlinear, showing a local minimum near $H \sim 2.5$ kOe. For $T = 2$ K $< T_c$, the $H_{c2}$ value is clearly higher than the 65 kOe maximum field we applied (see discussion and figures below). $H_{c1}$ can be inferred from the lower field $M(H)$ data.

To better estimate $H_{c1}$ values, we performed low field $M(H)$ sweeps at base temperature. In Fig. 11(a) we show the $M(H)$ data for $0 \leqslant x \leqslant 0.025$ for $H \leqslant 100$ Oe. As $x$ increases, the deviation from the fully shielded, linear behavior, that occurs at $H_{c1}$, appears at lower and lower fields. As shown in the inset of Fig. 11(a), $\Delta M$ is determined by subtracting the

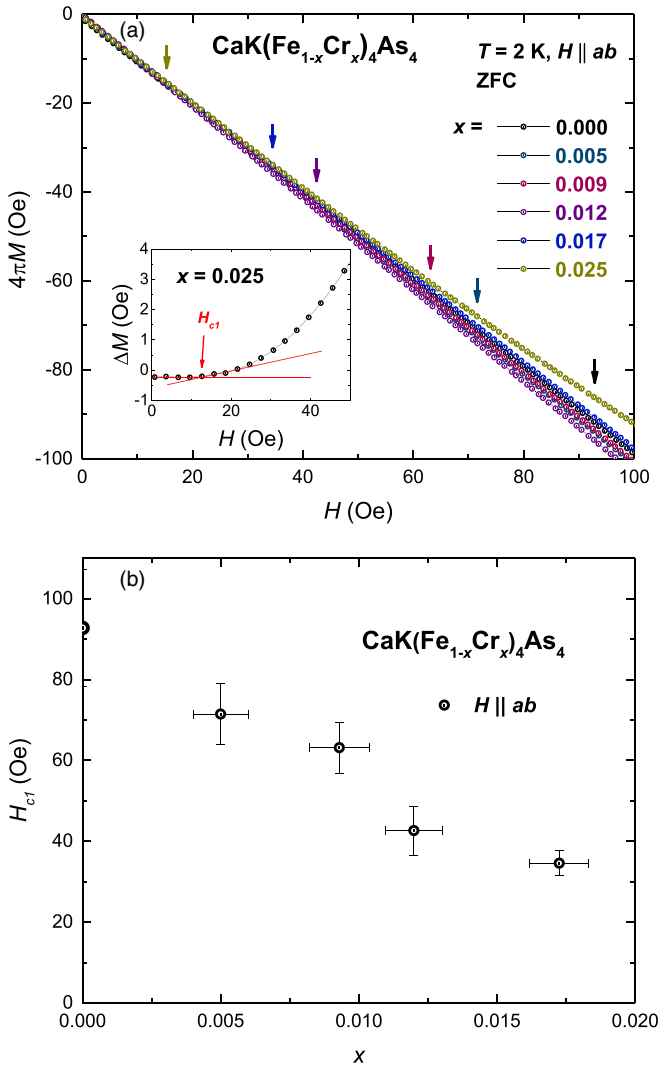


FIG. 11. (a) Magnetization as a function of magnetic field applied parallel to the crystallographic *ab* axis at 2 K for different substitution levels. Arrows mark the value of the magnetic field ($H_{c1}$) where $M(H)$ deviates from linear behavior. The inset shows the criterion we use to determine the $H_{c1}$ values. Remnant fields of measurements are smaller than 1 Oe, which is consistent with $M(H)$ plots shown in the figure. Demagnetization was performed at 60 K and then samples were cooled in zero field to 2 K to minimize the remnant magnetic field. (b) $H_{c1}$ values at 2 K vs $x$.

linear, lowest field behavior of $4\pi M$ from $H$. Figure 24 in the Appendix shows plots of $\Delta M$ as a function of field. Given the finite thickness of samples and field direction applied in the *ab* plane, there is a small demagnetizing factor ($N < 0.077$), therefore $H_{c1}$ is taken as the vortices start to enter the sample and is determined as the point when the $M(H)$ data deviate from the linear, lowest field behavior. The nonzero value is due to the remnant field of MPMS. The standard error of $H_{c1}$ comes from at least four different samples' measurements. Figure 11(b) shows $H_{c1}$ at 2 K with different substitution. $x = 0.025$ is not shown in this plot since $T_c \sim 7$ K is close to 2 K. The data shown in Fig. 11(b) are roughly linear in $x$. This will be discussed further when we examine the London penetration depth below.

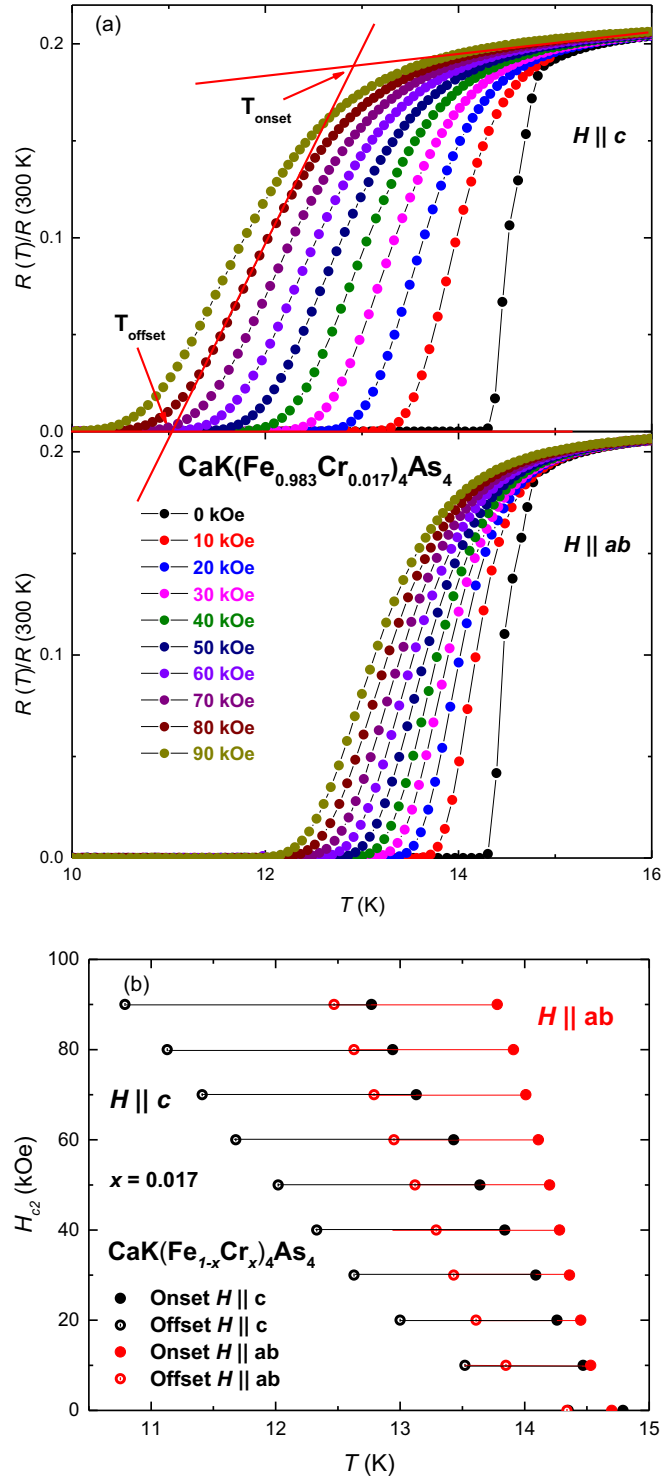


FIG. 12. (a) Temperature-dependent electrical resistance of $CaK(Fe_{0.983}Cr_{0.017})_4As_4$ single crystal for magnetic field parallel to the crystallographic *c* axis (upper panel) and *ab* plane (lower panel) for representative fields $H \leqslant 90$ kOe. Onset and offset criteria for $T_c$ are shown by the red solid lines. (b) Anisotropic $H_{c2}(T)$ data determined for two single crystalline samples of $CaK(Fe_{0.983}Cr_{0.017})_4As_4$ using onset criterion (solid) and offset criterion (hollow) inferred from the data shown in (a).

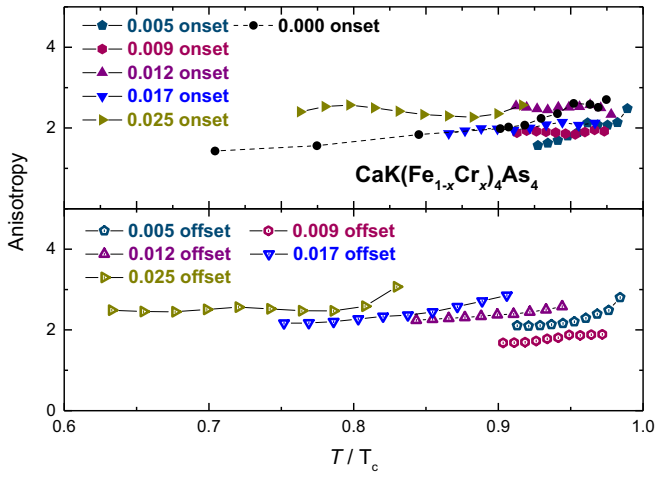


FIG. 13. Anisotropy of the upper critical field, $\gamma = H_{c2}^{\|ab}(T)/H_{c2}^{\|c}(T)$, as a function of effective temperature, $T/T_c$, for $CaK(Fe_{1-x}Cr_x)_4As_4$ single crystals, using onset criterion (upper panel) and offset criterion (lower panel), inferred from the temperature-dependent electrical resistance data. The $T_c$ value used to calculate the effective temperature ($T/T_c$) is the zero-field superconductivity transition temperature for each Cr-substitution level (see Fig. 8 above). Data $CaKFe_4As_4$ are shown in black circles with a dashed line.

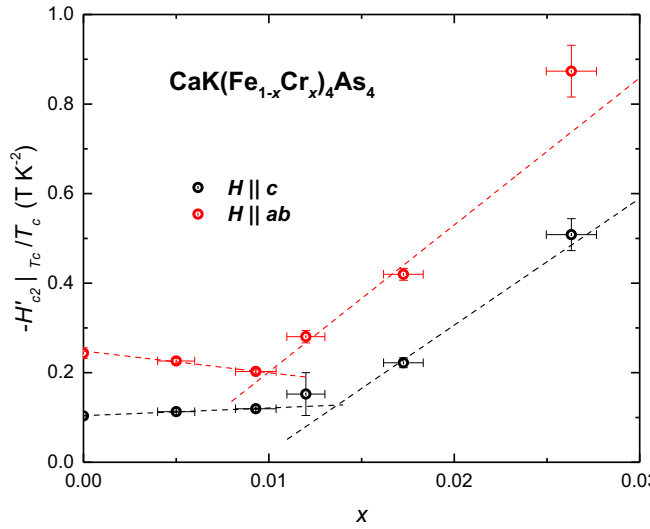


FIG. 14. Substitution dependence of the slope of $H_{c2}(T)$ at $T_c$, $-H'_{c2}(T)/T_c$, where $H'_{c2}(T)$ is $dH_{c2}(T)/dT$ at $T_c$. $T_c$ is determined by $T_{\text{offset}}$ from criteria shown in Fig. 12. Qualitatively similar, albeit somewhat weaker, results can be seen using $T_{\text{onset}}$ criterion data. Dashed lines show the linear fit for $x < 0.01$ and $x > 0.01$, which indicate the change of trend of $H_{c2}(T)$ at $T_c$ vs $x$ as substitution increases.

To further study the effects of Cr substitution on the superconducting state, anisotropic $H_{c2}(T)$ data for temperatures near $T_c$ were determined for the substitution levels that have superconductivity. Figure 12(a) shows a representative set of $R(T)$ data taken for fixed applied magnetic fields, $H \parallel c$ axis, and $ab$ plane $\leqslant 90$ kOe for $x = 0.017$. Figure 12(a) also shows an example of the onset and offset criteria used for the evaluation of $T_c$. Figure 12(b) presents the anisotropic $H_{c2}(T)$ curves for $CaK(Fe_{0.983}Cr_{0.017})_4As_4$ single crystals with both $H||c$ and $H||ab$, showing both the onset ($T_{\text{onset}}$) and offset ($T_{\text{offset}}$) temperatures. For $x = 0.005$, 0.009, 0.012, and 0.025, $H_{c2}(T)$ curves are shown in the Appendix, Figs. 25–28. From $H_{c2}(T)$ plots, we can see that $T_c$ is only suppressed by about 4 K when 90 kOe magnetic field is applied, so the complete $H_{c2}(T)$ plots of the $CaK(Fe_{1-x}Cr_x)_4As_4$ compounds cannot be fully determined, however we can still observe several trends in these data.

Figure 13 shows that the temperature-dependent anisotropy ratio, $\gamma = H_{c2}^{\|ab}(T)/H_{c2}^{\|c}(T)$, is around 2.5 for these samples over the $0.6 < T/T_c < 1.0$ range. This value is similar to other 122 and 1144 materials [6,15,21,34]. $\gamma \sim 2.5$ is also qualitatively consistent with the estimated resistivity anisotropy ratio $\gamma_\rho = \rho_c/\rho_a \approx 3$–6 at 300 K, increasing to 6–10 at $T = 0$ K, with $\gamma_H \sim \sqrt{\gamma_\rho}$ [38]. Black circles and the dashed line present the data for pure $CaKFe_4As_4$ [6]. The anisotropies of coherence length and penetration depth are expected to be the same close to $T_c$, but they can have opposite temperature dependence upon cooling below that [39]. However, almost no temperature dependence of $\gamma$ is seen in the temperature range measured.

Given that we have determined $H_{c2}(T)$ for temperatures close to $T_c$, we can evaluate the $H'_{c2}(T)/T_c$ close to $T_c$, where $H'_{c2}(T)$ is $dH_{c2}(T)/dT$, specifically seeing how it changes as $T_c$ drops below $T^*$ with increasing $x$. Error of $H'_{c2}(T)/T_c$ comes from a linear fit of $H_{c2}(T)$ near the $T_c$. In the case of other Fe-based systems [21,40–43], clear changes in $H'_{c2}(T)/T_c$ were associated with changes in the magnetic sublattice coexisting with superconductivity (i.e., ordered or disordered). In Fig. 14 we can see that there is a change in the $x$-dependence of $H'_{c2}(T)/T_c$ for $x > 0.012$, beyond which the substitution level suppresses $T_c$ below $T^*$. Comparison with the slope change of $H_{c2}$ in the pressure-temperature phase diagram of $CaK(Fe_{1-x}Ni_x)_4As_4$ [40] further suggests that this is probably related to changes in the Fermi surface, caused by the onset of the new periodicity associated with the AFM order.

## VI. DISCUSSION AND SUMMARY

The $T$-$x$ phase diagram for $CaK(Fe_{1-x}Cr_x)_4As_4$ (Fig. 8) is qualitatively similar to those found for Co-, Ni-, and Mn-substituted $CaKFe_4As_4$. There is a clear suppression of $T_c$ with increasing Cr substitution as well as an onset of what is likely to be an AFM ordering for $x > 0.012$.

In Figs. 11 and 14 we presented measurements and analysis of $H_{c1}$ and $H_{c2}$ data. Whereas we see only a subtle, if any, effect of the onset of AFM ordering on $H_{c1}$ [Fig. 11(b)], there is a clear effect on $H_{c2}$ (Fig. 14). Using our $H_{c1}$ and $H_{c2}$ data, we can extract information about the superconducting coherence length and London penetration depth as well.

Figure 15(a) shows the coherence length, $\xi$, of $CaK(Fe_{1-x}Cr_x)_4As_4$ as a function of $x$. $\xi$ is estimated by using the anisotropic scaling relations $0.69|dH_{c2}^{||c}/dT| = \phi_0/2\pi\xi_{ab}^2 T_c$ and $0.69|dH_{c2}^{\perp c}/dT| = \phi_0/2\pi\xi_c\xi_{ab}T_c$ [6]. We estimate $H_{c2}(0)$ with $H_{c2}(0)/[T_c|dH_{c2}(T_c)/dT|] = 0.69$ [44]. Figure 15(b) shows the London penetration depth,

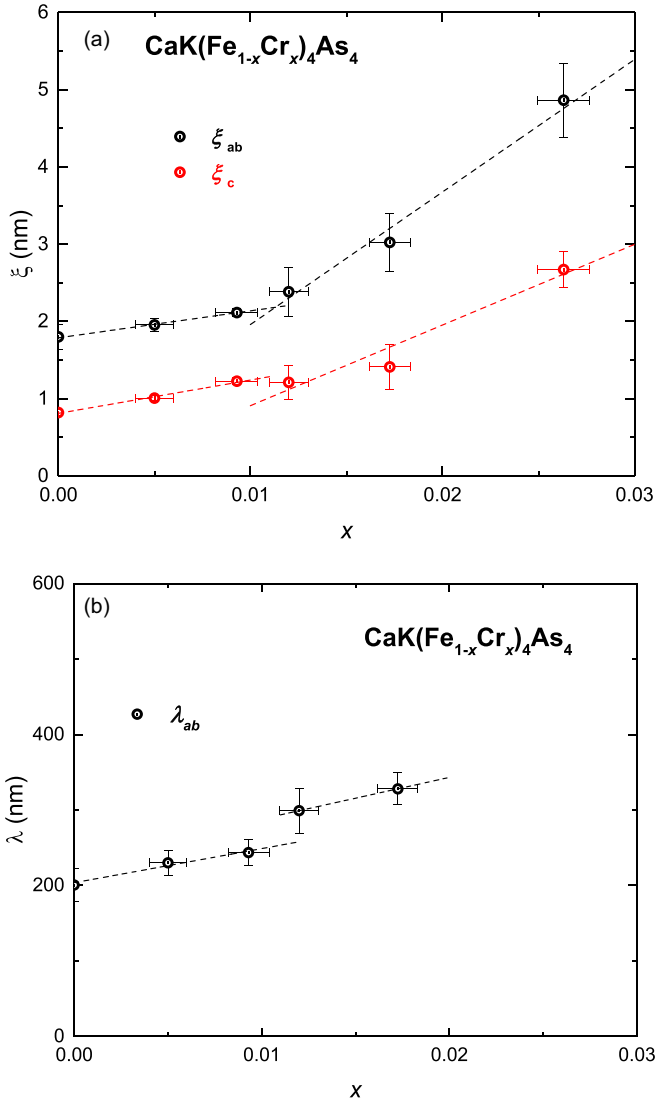


FIG. 15. (a) Coherence length vs $x$ plot of $CaK(Fe_{1-x}Cr_x)_4As_4$ single crystals with applied field in the $c$ direction and the $ab$ plane. Part (b) shows the London penetration depth as a function of $x$ obtained by magnetic field applied parallel to the crystallographic $ab$ axis with different substitution levels. Dashed lines show the linear fit for $x < 0.01$ and $x > 0.01$, which show the change of coherence lengths and London penetration depths at $T_c$ vs $x$ as substitution increases.

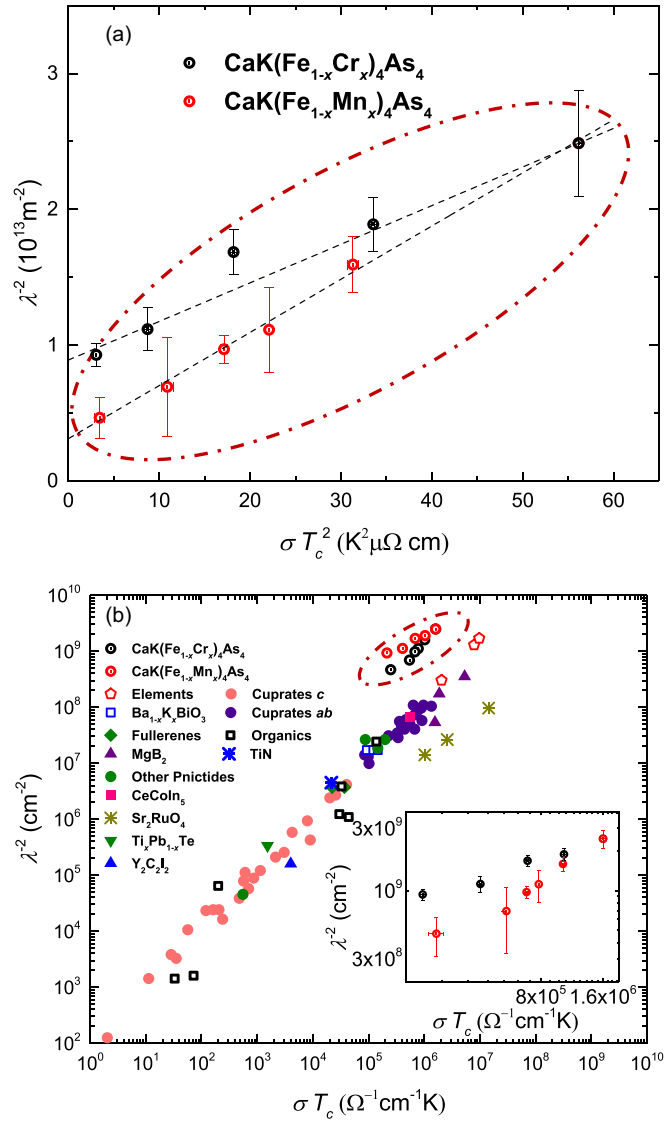


FIG. 16. Part (a) shows $\lambda^{-2}$ vs $\sigma\ T_c^2$ (modified Homes scaling [55]) of Cr (black) and Mn (red) substitution of $CaKFe_4As_4$. Dashed lines show the linear fits of $CaK(Fe_{1-x}Mn_x)_4As_4$ data with free parameter (red) and $CaK(Fe_{1-x}Cr_x)_4As_4$ data with a fixed point at $x = 0$ (black). Part (b) shows Homes' scaling ($\lambda^{-2}$ vs $\sigma T_c$) with other superconductors [56]. Except for $CaK(Fe_{1-x}Cr_x)_4As_4$ and $CaK(Fe_{1-x}Mn_x)_4As_4$, Homes' scaling is given by $1/\lambda_s^2 \propto T_c\sigma_{dc}$. $\sigma_{dc}$ is DC conductivity, and data points are obtained from optical spectroscopes. Red dash-dotted ellipse marks the Mn- and Cr-substituted 1144 data points. The inset shows Homes' scaling of $CaK(Fe_{1-x}Cr_x)_4As_4$ (black) and $CaK(Fe_{1-x}Mn_x)_4As_4$ (red).

$\lambda_{ab}$, as a function of $x$. According to Fig. 11(a), $H_{c1}$ is measured at 2 K, and $x = 0.025$, $T_c \sim 7$ K, will not be counted since we want to compare the similar $T/T_c$ values of $CaK(Fe_{1-x}Cr_x)_4As_4$ samples. We estimate the anisotropy of coherence length ($\gamma_\xi = 1$ [45–47]) and the penetration depth ($\gamma_\lambda = 2.5$ [48,49]) in the low-temperature limit. According to Fig. 13, $\gamma$ is not changed much near $T_c$ as the substitution level changes; based on that, we assume the substituted samples have the same anisotropy as the pure sample. $\lambda_{ab}$ is obtained by using

$$H_{c1}^{\|ab} = \phi_0/(4\pi\lambda_{ab}\lambda_c)(\ln\kappa_{ab} + 0.5) \quad (1)$$

$$= \phi_0/\left(4\pi\lambda_{ab}^2\gamma_\lambda\right)[\ln(\lambda_{ab}/\xi_{ab}) + 0.5\ln\gamma_\lambda + 0.5], \quad (2)$$

$\lambda_c/\lambda_{ab} = \gamma_\lambda$, $\xi_{ab}/\xi_c = H_{c2}^{\|ab}(T)/H_{c2}^{\|c}(T) = \gamma_\xi$, and $\kappa_{ab} = \sqrt{\lambda_{ab}\lambda_c/\xi_{ab}\xi_c}$ [50–52]. The penetration depth, $\lambda_{ab} = 200 \pm 22$ nm, obtained using Eq. (2) of $CaKFe_4As_4$ is very close to the values from $\mu$SR and the self-oscillating tunnel-diode resonator measurements [48,53,54]. Coherence lengths and penetration depths increase as substitution levels increase, and given that $\xi$ depends on $dH_{c2}/dT$, penetration depths depend on $H_{c1}$ and $\xi$. Both Figs. 15(a) and 15(b) show breaks in behavior near $x \sim 0.01$, the substitution level at which $T^*$ emerges from below $T_c$.

Figure 16(a) shows $\lambda^{-2}$ versus $\sigma\ T_c^2$ in Cr and Mn substitution of $CaKFe_4As_4$, where $\sigma$ is normal state conductivity, which was measured just before $T_c$ (resistivity plot is shown in the Appendix, Fig. 20). Both $CaK(Fe_{1-x}Cr_x)_4As_4$ and $CaK(Fe_{1-x}Mn_x)_4As_4$ data roughly follow the linear behavior associated with the modified Homes-type scaling in the presence of pair breaking [55,57]. However, the slopes of the linear fits are slightly different. Figure 16(b) shows the Homes scaling of superconductors on a log-log scale [56]. Other pnictides are $Ba(Fe_{0.92}Co_{0.08})_4As_4$ and $Ba(Fe_{0.95}Ni_{0.05})_4As_4$. Cuprates are $YBa_2Cu_3O_{6+y}$. On this log-log scale, both the $CaK(Fe_{1-x}Cr_x)_4As_4$ and $CaK(Fe_{1-x}Mn_x)_4As_4$ data sets agree rather well with other data, although they are somewhat shifted up. It should be noted that the other data were determined from optical measurements [56], and differences in criteria as well as measurement techniques may be responsible for the offset.

The $T$-$x$ phase diagrams of $T$ = Co and Ni substitutions in $CaK(Fe_{1-x}T_x)_4As_4$ scaled almost exactly as a function of band-filling change (i.e., when each Ni atom brings two extra electrons and each Co atom brings only one extra electron) [18,23]. This led to the conclusion that for electron doping of $CaKFe_4As_4$, the number of electrons added was the control parameter for both the stabilization of magnetic ordering as well as for the suppression of superconductivity. This scaling did not seem to work for the case of Mn substitution [21], but with only one "holelike" transition-metal substitution it was hard to make clear conclusions.

When Cr is substituted into $CaKFe_4As_4$, though, there is a qualitatively similar suppression of superconductivity as well as the stabilization of magnetic order, as was found for $T$ = Mn, Co, and Ni. However, there is a clear and important difference on a quantitative level, as shown in Fig. 17(a). The $T$-$x$ phase diagram of $CaK(Fe_{1-x}Cr_x)_4As_4$ is essentially identical to that of $CaK(Fe_{1-x}Mn_x)_4As_4$. This is very different behavior from [Fig. 17(b)] that seen for electron-doped 1144, where electron count seemed to be the key variable.

In Fig. 17(c), the $CaK(Fe_{1-x}T_x)_4As_4$ phase diagrams for $T$ = Cr, Mn, Co, and Ni are plotted on the same $T$ and $\Delta e^-$ axes. Comparison of Figs. 17(a), 17(b) and 17(c) reveals a clear and striking difference between the hole- and electron-doped $CaK(Fe_{1-x}T_x)_4As_4$ systems. Whereas for the electron-doped system ($T$ = Co,Ni) there is very clear scaling with the number of added electrons, for the hole-doped system ($T$ = Mn,Cr) there is clear scaling with the number of substituted atoms, $x$. These striking differences in the phase diagrams beg the question of what is different between the two types of substitution. When there were only data on Mn substitution to compare with the Co and Ni substitutions, one possible explanation could be based on an asymmetric density of electronic states on either side of $E_F$. Given that the Cr- and Mn-substituted phase diagrams scale with $x$ rather than $e^-$, this is no longer a possibility.

A different approach to these data is to note that there is one other clear difference between the Mn and Cr substitutions as compared to the Co and Ni ones. Mn and Cr clearly bring local-moment-like behavior as manifest by their conspicuous, high temperature, Curie tails that grow with increasing $x$. This is absent for the Co and Ni substitutions. The effective moments coming from the Mn and Cr Curie tails

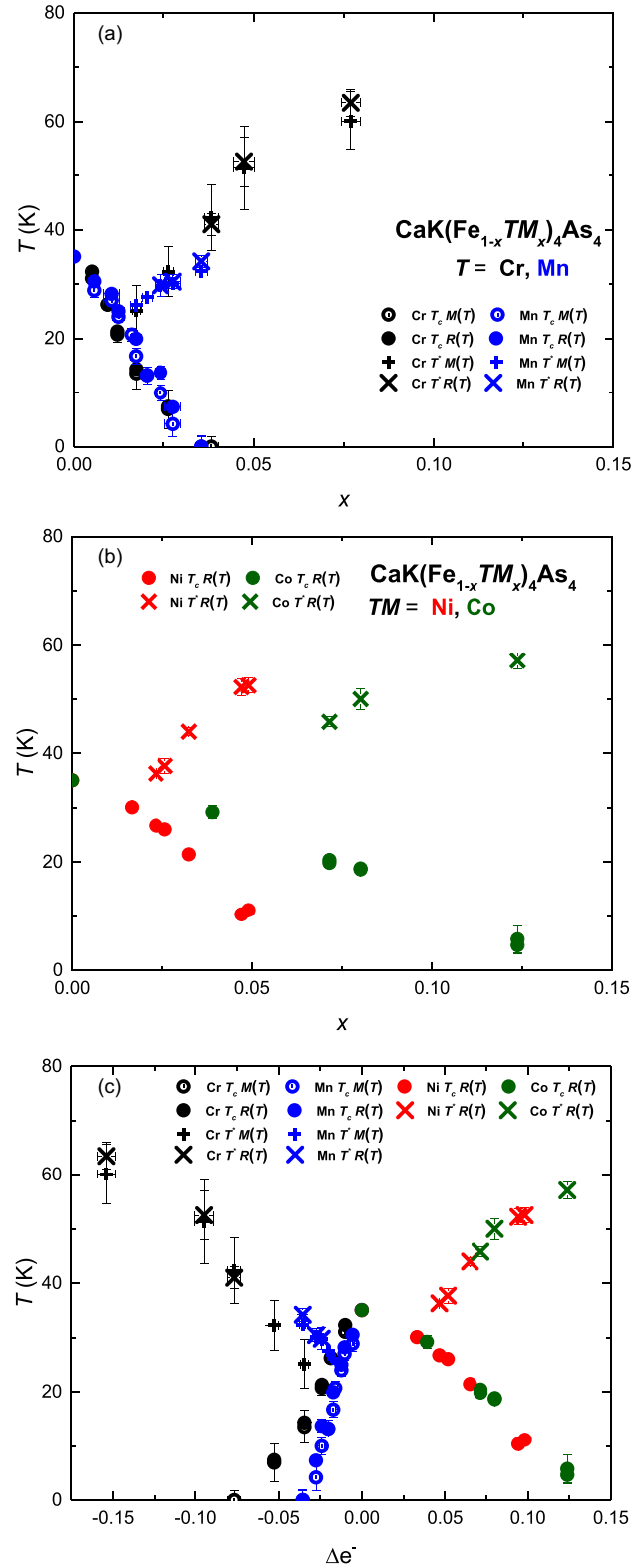


FIG. 17. (a),(b) Temperature vs substitution level $x$ phase diagram of $CaK(Fe_{1-x}T_x)_4As_4$ single crystals, $T$ = Cr, Mn, Ni, and Co [18]. (c) Temperature vs $\Delta e^-$ change of electrons phase diagram of $CaK(Fe_{1-x}T_x)_4As_4$ single crystals, $T$ = Cr, Mn, Ni, and Co. The circular symbols denote the $T_c$ phase transitions, and the crosslike symbols denote the $T^*$ and $T_N$ phase transitions, which are obtained from resistance and magnetic moment measurements, denoted as "$R(T)$" and "$M(T)$."

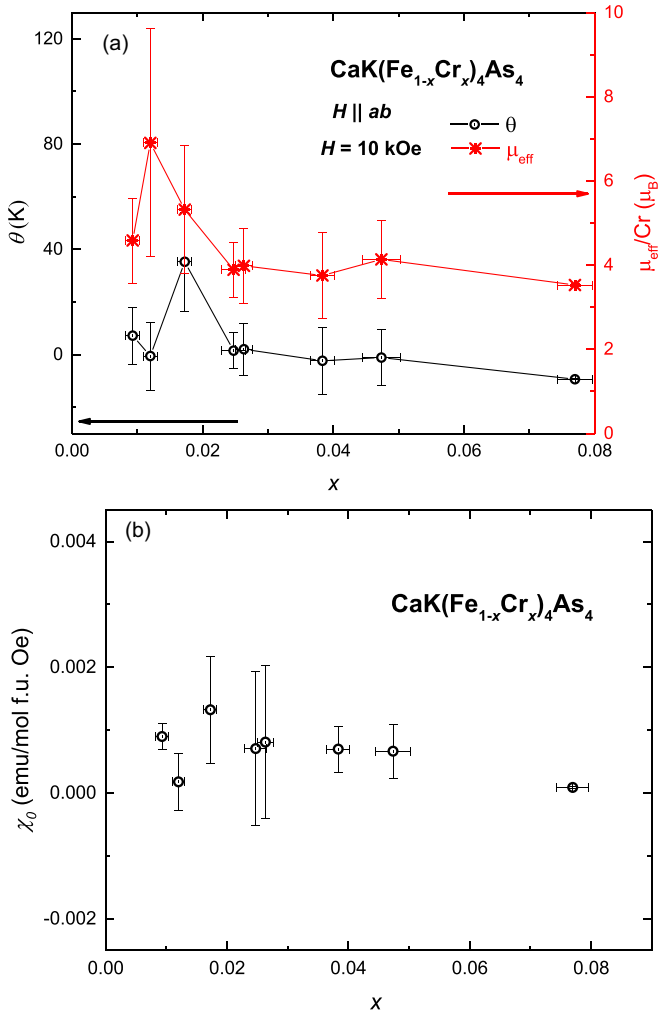


FIG. 18. Part (a) shows Curie-Weiss temperature, $\theta$, effective moment, $\mu_{\text{eff}}$, obtained from Curie-Weiss fit to the difference magnetization ($\Delta M'$) between $CaKFe_4As_4$ and $CaK(Fe_{1-x}Cr_x)_4As_4$ single crystals as a function of temperature for a field of 10 kOe applied parallel to the crystallographic *ab* plane. Part (b) shows temperature-independent susceptibility, $\chi_0$.

($\sim 5\mu_B$ [21] and $\sim 4\mu_B$, respectively) are consistent with $Mn^{3+}$ and $Cr^{3+}$ valences. The Cr and Mn appear to behave like local moment impurities. As such, it is not surprising that they lead to a stronger suppression of $T_c$ (via Abrikosov-Gor'kov pair breaking [58]). In a similar manner, it is not surprising that the addition of relatively large, local moment impurities to an itinerant, relatively small moment system helps to stabilize magnetic order. Given that the sizes of the local moments are similar, it is not surprising that we find that the $T$-$x$ phase diagrams scale well. The fact that $CaKFe_4As_4$ manifests rather bimodal responses to $T$ substitution for $T$ = Co and Ni versus $T$ = Mn and Cr is consistent with the growing understanding of many of the Fe-based superconductor [15,59] families as manifesting properties in between those of a wide band metal (which would support rigid band shifting) and a more ionic-like or Zintl-like compound (that would support valence-counting-like behavior).

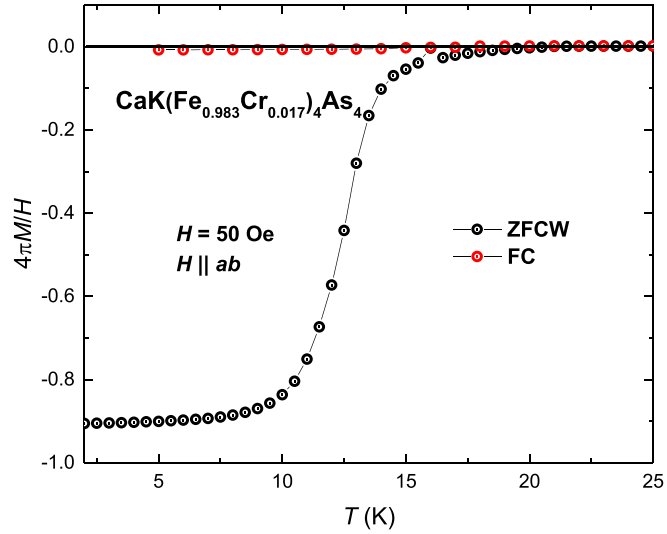


FIG. 19. Zero-field-cooled-warming (ZFCW) and field-cooled (FC) low-temperature magnetization as a function of temperature for $CaK(Fe_{0.983}Cr_{0.017})_4As_4$ single crystals with a field of 50 Oe applied parallel to the crystallographic *ab* plane. $M$ is the volumetric magnetic moment with cgs unit emu $cm^{-3}$ or Oe.

In summary, we have been able to grow and study the $CaK(Fe_{1-x}Cr_x)_4As_4$ system. Based on magnetic and transport measurements, we assemble a $T$-$x$ phase diagram that clearly shows the suppression of the superconducting $T_c$ with the addition of Cr, with $T_c$ dropping from 35 K for $x = 0$ to zero for $x \sim 0.03$, as well as the stabilization of magnetic order for $x > 0.012$, with $22 \leqslant T^* \leqslant 60$ K. As $x$ becomes greater than 0.012 and $T_c$ becomes less than $T^*$, a clear change in the behavior of $H'_{c2}(T)/T_c$ and the associated superconducting coherence length, $\xi$, can be seen. These are associated with the probable changes in the Fermi surface

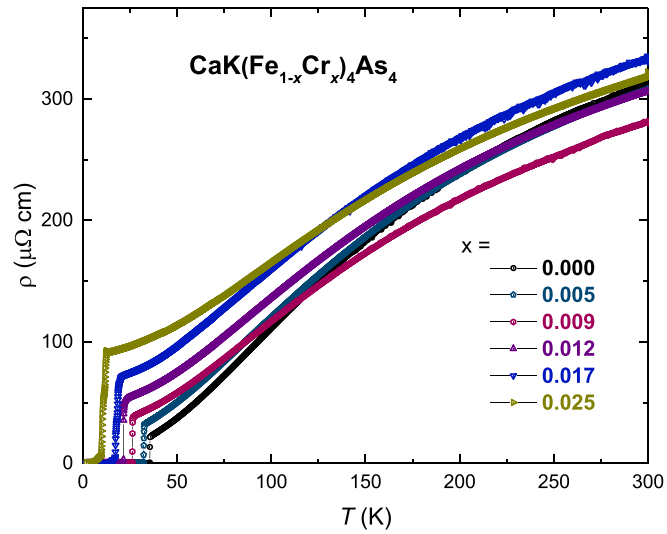


FIG. 20. Temperature dependence of resistivity, $\rho$, of $CaK(Fe_{1-x}Cr_x)_4As_4$ single crystals showing the suppression of the superconducting transition $T_c$.

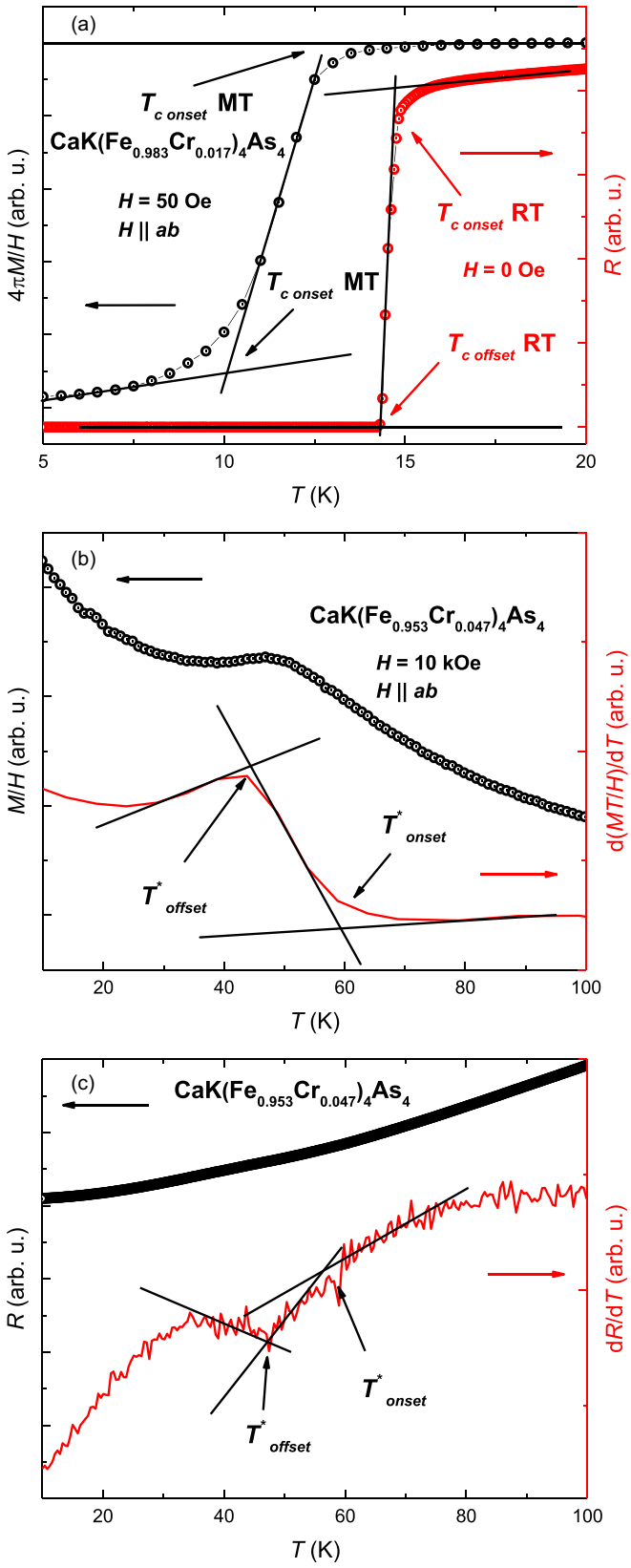


FIG. 21. Onset and offset criteria for $T_c$ and $T^*$ based on magnetization and resistance measurement.

that accompany the AFM ordering at $T^*$. Comparable features in $H_{c1}$ or the London penetration depth are not clearly resolvable.

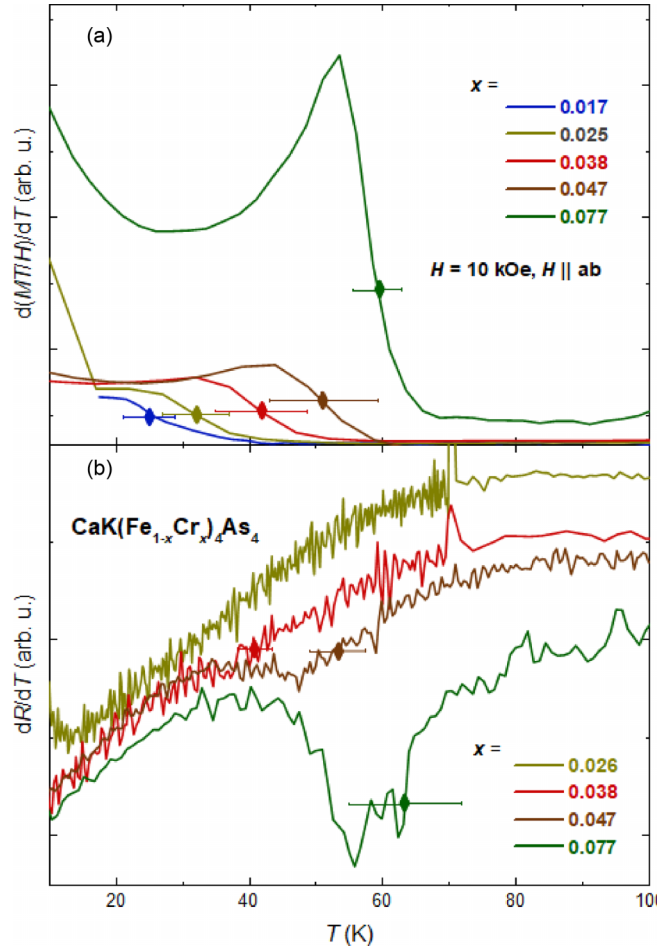


FIG. 22. The $T^*$ anomaly appears clearly as a step in both plot $d(MT/H)/dT$ and the derivative of resistance, $dR/dT$. Only the data above $T_c$ are plotted. Rhombus symbols show the transition temperature of $T^*$, and error bars come from the criteria introduced above.

The $T$-$x$ phase diagram for CaK$(Fe_{1-x}Cr_x)_4As_4$ is qualitatively identical to CaK$(Fe_{1-x}Mn_x)_4As_4$ phase diagram due to the effect of the local moment of Cr and Mn. The similarity of the phase diagrams also indicates the importance of the local moment impurity on the hole-doped 1144, which is different from the electron-doped 1144. On the other hand, both hole and electron doping in 1144 stabilize antiferromagnetic ordering with increasing substitution level, and the suppression of $T_c$ in CaK$(Fe_{1-x}Cr_x)_4As_4$ is faster than Ni- and Co-1144.

## ACKNOWLEDGMENTS

We thank B. Kuthanazhi for useful discussions. Work at the Ames National Laboratory was supported by the U.S. Department of Energy, Office of Science, Basic Energy Sciences, Materials Sciences and Engineering Division. The Ames National Laboratory is operated for the U.S. Department of Energy by Iowa State University under Contract No. DE-AC02-07CH11358.

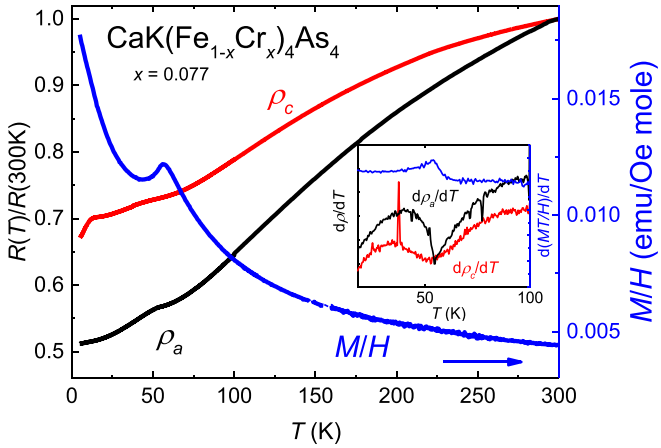


FIG. 23. Temperature dependence of normalized resistance, $R(T)/R(300\ \mathrm{K})$, of $CaK(Fe_{1-x}Cr_x)_4As_4$ single crystals with $x = 0.077$ for electrical currents along the $a$-axis (black) and along the $c$-axis (red). Magnetic susceptibility shows a clearly distinguished anomaly, similar to the features observed in raw resistivity data for both current directions. The inset shows resistivity derivatives plotted against $d(MT/H)/dT$ (blue). The onset of the feature in the $d(MT/H)/dT$ curve at ~50 K is accompanied by the clear feature in both $c$- and $a$-axis resistivity derivatives.

## APPENDIX

The magnetization plots shown in Fig. 4 have the appearance of Curie-Weiss tails potentially associated with the Cr-substitution. We fit the magnetization difference ($\Delta M'$) between $CaK(Fe_{1-x}Cr_x)_4As_4$ and $CaKFe_4As_4$ single crystals as a function of temperature from 20 K above $T_c$ to 250 K with a field of 10 kOe applied parallel to the crystallographic $ab$ plane by a $C/(T+\theta) + \chi_0$ function assuming that tail behavior

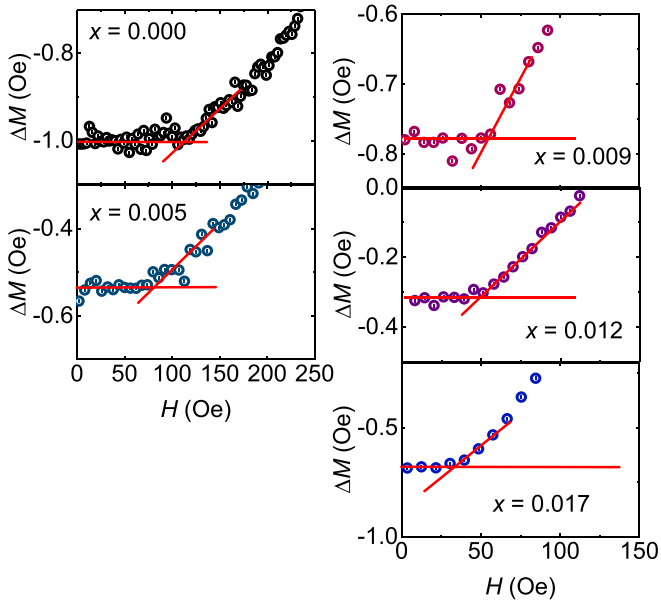


FIG. 24. The criterion to determine the $H_{c1}$ values for different substitutions. The remnant field of measurements is smaller than 1 Oe. Demagnetization was performed at 60 K and then samples were cooled in zero field to 2 K to minimize the remnant magnetic field.

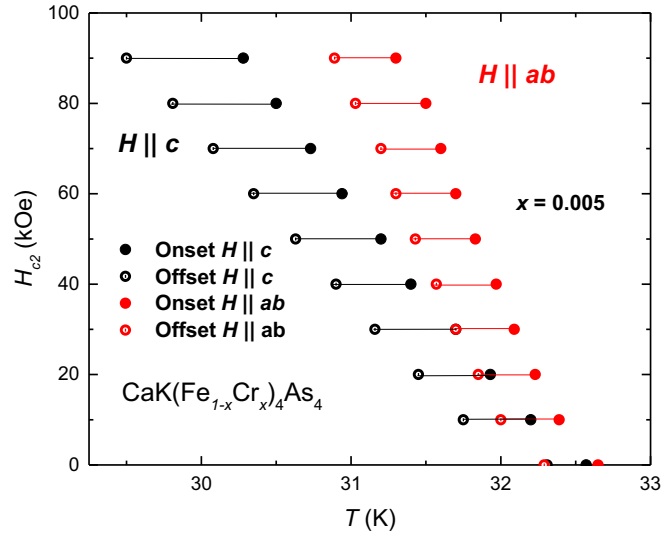


FIG. 25. Anisotropic $H_{c2}(T)$ data determined for two single crystalline samples of $x_{EDS} = 0.005$ $CaK(Fe_{1-x}Cr_x)_4As_4$ using onset criterion (solid) and offset criterion (hollow) inferred from the temperature-dependent electrical resistance data.

is only due to Cr. Figure 18 shows the result of fitting. The value of $\mu_{eff}$ is around $4\mu_B$. The fitting results comes from at least four different sample $M(T)$ measurements. The values of $\theta$, $\mu_{eff}$, and $\chi_0$ become more stable after $x = 0.17$. Instability for small substitution levels may come from the difficulty of fitting a small tail-like contribution, and when $x = 0.005$ there is no clear tail shown.

Figure 19 shows zero-field-cooled-warming (ZFCW) and field-cooled-warming (FC) low-temperature magnetization as a function of temperature for $CaK(Fe_{0.983}Cr_{0.017})_4As_4$ single crystals with a field of 50 Oe applied parallel to the $ab$ plane.

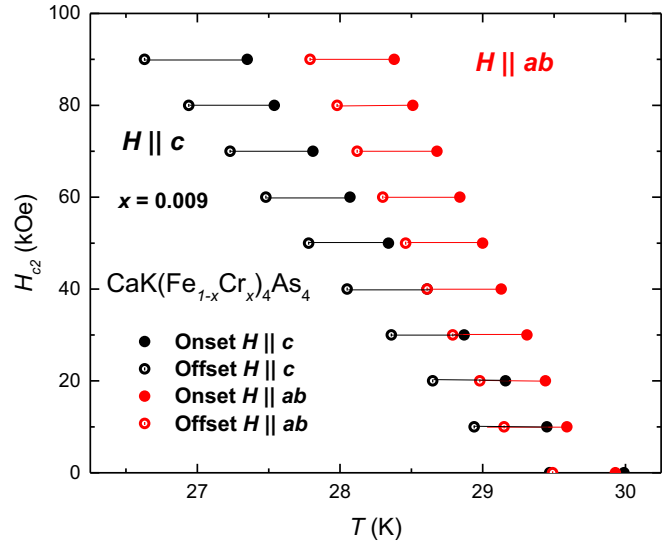


FIG. 26. Anisotropic $H_{c2}(T)$ data determined for two single-crystalline samples of $x_{EDS} = 0.009$ $CaK(Fe_{1-x}Cr_x)_4As_4$ using onset criterion (solid) and offset criterion (hollow) inferred from the temperature-dependent electrical resistance data.

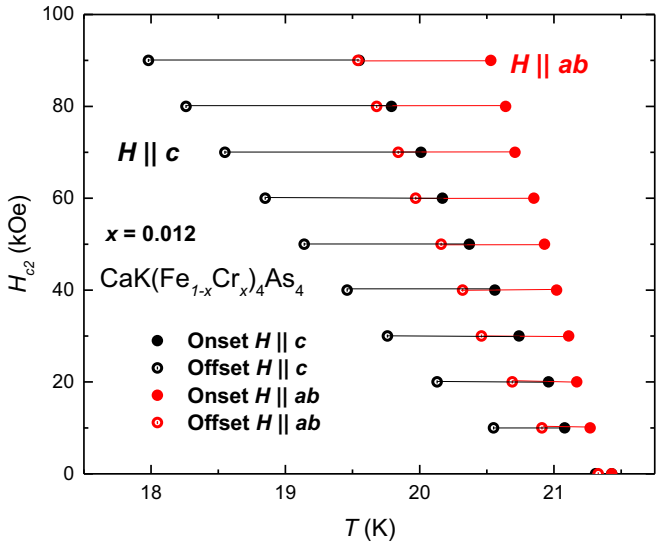


FIG. 27. Anisotropic $H_{c2}(T)$ data determined for two single-crystalline samples of $x_{\mathrm{EDS}} = 0.012$ $\mathrm{CaK(Fe_{1-x}Cr_x)_4As_4}$ using onset criterion (solid) and offset criterion (hollow) inferred from the temperature-dependent electrical resistance data.

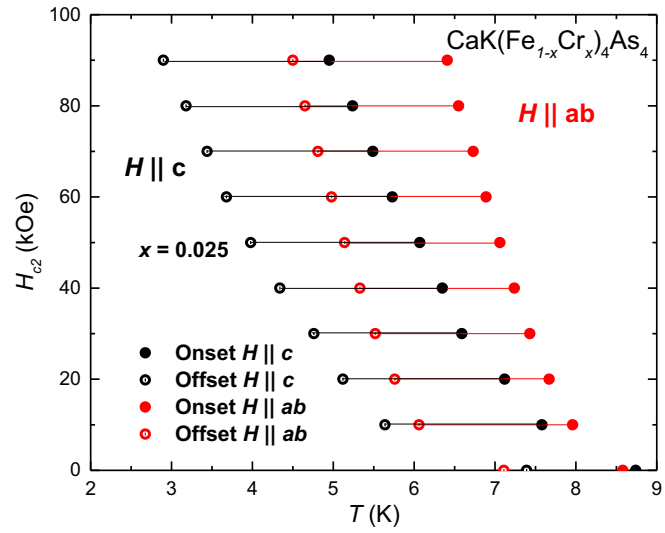


FIG. 28. Anisotropic $H_{c2}(T)$ data determined for two single-crystalline samples of $x_{\mathrm{EDS}} = 0.025$ $\mathrm{CaK(Fe_{1-x}Cr_x)_4As_4}$ using onset criterion (solid) and offset criterion (hollow) inferred from the temperature-dependent electrical resistance data.

The large difference between ZFCW and FCW is consistent with the large pinning found even in pure $\mathrm{CaKFe_4As_4}$ [60].

Figure 20 shows the temperature dependence of resistivity, $\rho$, of $\mathrm{CaK(Fe_{1-x}Cr_x)_4As_4}$ single crystals with $x < 0.38$. Thickness is estimated by the density of pure $\mathrm{CaKFe_4As_4}$, the mass and area of platelike samples. The superconducting transition temperature is suppressed, and resistivity before $T_c$ is increased by increasing substitution. Given the inevitably large geometric errors associated with the precise determination of length between voltage contacts as well as the sample thickness, we consider the uncertainty in our resistivity values to be on the order of 20%, and as such we plot the data as $R(T)/R(300\ \mathrm{K})$ in the main text.

Criteria for inferring $T_c$ and $T^*$ are shown in Fig. 21. For $T_c$ [Fig. 21(a)] we use an onset criterion for $M(T)$ data and an offset criterion for $R(T)$ data. As is often the case, these criteria agree well, especially in the low-field limit. The error bar of $T_c$ is determined by half of the difference between onset and offset. Since according to Ref. [36], $d(\chi T)/dT$, $d(\rho)/dT$ behave like $C_p$, which gives the transition temperature between onset and offset points, we use the average of onset and offset values of $d(\chi T)/dT$ and $d(\rho)/dT$ as $T^*$. For $T^*$, although the feature is much clearer for Cr substitution than it was for Mn, Ni, or Co substitutions [18,21], the features in $M(T)$ and $R(T)$ are still somewhat subtle in the low substitution level. We infer $T^*$ as the average of onset and offset values, and we use half of the difference between onset and offset as the error.

$dR(T)/dT$ and $dM(T)/dT$ data for several different $x$-values are shown in Fig. 22, showing good agreement between the position of the $T^*$ features. The temperature dependence of normalized resistance is shown in Fig. 23. Figure 24 shows the criterion used to determine the $H_{c1}$ values for the samples with different substitutions levels. We average at least four $H_{c1}$ values from the different samples of the same substitution level.

Figures 25–28 present $H_{c2}(T)$ curves, which are obtained from $R(T)$ data for fixed applied fields and the criteria shown in Fig. 12(a) of $\mathrm{CaK(Fe_{1-x}Cr_x)_4As_4}$ single crystals for $x = 0.005$, 0.009, 0.012, 0.017, and 0.025.


[1] Y. Kamihara, T. Watanabe, M. Hirano, and H. Hosono, J. Am. Chem. Soc. **130**, 3296 (2008).

[2] D. C. Johnston, Adv. Phys. **59**, 803 (2010).

[3] J. Paglione and R. L. Greene, Nat. Phys. **6**, 645 (2010).

[4] H. Hosono and K. Kuroki, Physica C **514**, 399 (2015).

[5] A. Iyo, K. Kawashima, T. Kinjo, T. Nishio, S. Ishida, H. Fujihisa, Y. Gotoh, K. Kihou, H. Eisaki, and Y. Yoshida, J. Am. Chem. Soc. **138**, 3410 (2016).

[6] W. R. Meier, T. Kong, U. S. Kaluarachchi, V. Taufour, N. H. Jo, G. Drachuck, A. E. Böhmer, S. M. Saunders, A. Sapkota, A. Kreyssig *et al.*, Phys. Rev. B **94**, 064501(R) (2016).

[7] W. R. Meier, T. Kong, S. L. Bud'ko, and P. C. Canfield, Phys. Rev. Mater. **1**, 013401 (2017).

[8] F.-C. Hsu, J.-Y. Luo, K.-W. Yeh, T.-K. Chen, T.-W. Huang, P. M. Wu, Y.-C. Lee, Y.-L. Huang, Y.-Y. Chu, D.-C. Yan *et al.*, Proc. Natl. Acad. Sci. (USA) **105**, 14262 (2008).

[9] K. Kawashima, T. Kinjo, T. Nishio, S. Ishida, H. Fujihisa, Y. Gotoh, K. Kihou, H. Eisaki, Y. Yoshida, and A. Iyo, J. Phys. Soc. Jpn. **85**, 064710 (2016).

[10] J.-K. Bao, K. Willa, M. P. Smylie, H. Chen, U. Welp, D. Y. Chung, and M. G. Kanatzidis, Cryst. Growth Des. **18**, 3517 (2018).

[11] Z.-C. Wang, C.-Y. He, S.-Q. Wu, Z.-T. Tang, Y. Liu, A. Ablimit, C.-M. Feng, and G.-H. Cao, J. Am. Chem. Soc. **138**, 7856 (2016).

[12] Z.-C. Wang, C.-Y. He, S.-Q. Wu, Z.-T. Tang, Y. Liu, and G.-H. Cao, Chem. Mater. **29**, 1805 (2017).

[13] P. C. Canfield, S. L. Bud'ko, N. Ni, J. Q. Yan, and A. Kracher, Phys. Rev. B **80**, 060501(R) (2009).

[14] N. Ni, A. Thaler, A. Kracher, J. Q. Yan, S. L. Bud'ko, and P. C. Canfield, Phys. Rev. B **80**, 024511(R) (2009).

[15] N. Ni, A. Thaler, J. Q. Yan, A. Kracher, E. Colombier, S. L. Bud'ko, P. C. Canfield, and S. T. Hannahs, Phys. Rev. B **82**, 024519(R) (2010).

[16] P. C. Canfield and S. L. Bud'ko, Annu. Rev. Condens. Matter Phys. **1**, 27 (2010).

[17] G. R. Stewart, Rev. Mod. Phys. **83**, 1589 (2011).

[18] W. R. Meier, Q.-P. Ding, A. Kreyssig, S. L. Bud'ko, A. Sapkota, K. Kothapalli, V. Borisov, R. Valentí, C. D. Batista, P. P. Orth *et al.*, npj Quantum Mater. **3**, 5 (2018).

[19] A. E. Böhmer and A. Kreisel, J. Phys.: Condens. Matter **30**, 023001 (2018).

[20] E. Gati, L. Xiang, S. L. Bud'ko, and P. C. Canfield, Ann. Phys. **532**, 2000248 (2020).

[21] M. Xu, J. Schmidt, E. Gati, L. Xiang, W. R. Meier, V. G. Kogan, S. L. Bud'ko, and P. C. Canfield, Phys. Rev. B **105**, 214526 (2022).

[22] I. I. Mazin, Nature (London) **464**, 183 (2010).

[23] W. Meier, thesis (2018), https://lib.dr.iastate.edu/etd/16856/.

[24] A. Masi, A. Duchenko, G. Celentano, and F. Varsano, Supercond. Sci. Technol. **35**, 065015 (2022).

[25] P. C. Canfield, Rep. Prog. Phys. **83**, 016501 (2020).

[26] P. C. Canfield, T. Kong, U. S. Kaluarachchi, and N. H. Jo, Philos. Mag. **96**, 84 (2016).

[27] A. Jesche, M. Fix, A. Kreyssig, W. R. Meier, and P. C. Canfield, Philos. Mag. **96**, 2115 (2016).

[28] D. E. Newbury and N. W. M. Ritchie, in *Scanning Microscopies 2014*, edited by M. T. Postek, D. E. Newbury, S. F. Platek, and T. K. Maugel, International Society for Optics and Photonics (SPIE, 2014), Vol. 9236, p. 92360H.

[29] R. Prozorov and V. G. Kogan, Phys. Rev. Appl. **10**, 014030 (2018).

[30] M. A. Tanatar, N. Ni, S. L. Bud'ko, P. C. Canfield, and R. Prozorov, Supercond. Sci. Technol. **23**, 054002 (2010).

[31] M. A. Tanatar, R. Prozorov, N. Ni, S. L. Bud'ko, and P. C. Canfield, U.S. Patent (2013), https://patents.google.com/patent/US8450246B2.

[32] M. A. Tanatar, N. Ni, C. Martin, R. T. Gordon, H. Kim, V. G. Kogan, G. D. Samolyuk, S. L. Bud'ko, P. C. Canfield, and R. Prozorov, Phys. Rev. B **79**, 094507 (2009).

[33] M. A. Tanatar, N. Ni, G. D. Samolyuk, S. L. Bud'ko, P. C. Canfield, and R. Prozorov, Phys. Rev. B **79**, 134528 (2009).

[34] M. A. Tanatar, N. Ni, A. Thaler, S. L. Bud'ko, P. C. Canfield, and R. Prozorov, Phys. Rev. B **82**, 134528 (2010).

[35] J. M. Wilde, A. Sapkota, Q. P. Ding, M. Xu, W. Tian, S. L. Bud'ko, Y. Furukawa, A. Kreyssig, and P. C. Canfield, arXiv:2301.06336, 2023.

[36] M. E. Fisher, Philos. Mag. **7**, 1731 (1962).

[37] S. L. Bud'ko, V. G. Kogan, R. Prozorov, W. R. Meier, M. Xu, and P. C. Canfield, Phys. Rev. B **98**, 144520(R) (2018).

[38] J. Murphy, M. A. Tanatar, D. Graf, J. S. Brooks, S. L. Bud'ko, P. C. Canfield, V. G. Kogan, and R. Prozorov, Phys. Rev. B **87**, 094505(R) (2013).

[39] V. G. Kogan, R. Prozorov, and A. E. Koshelev, Phys. Rev. B **100**, 014518(R) (2019).

[40] L. Xiang, W. R. Meier, M. Xu, U. S. Kaluarachchi, S. L. Bud'ko, and P. C. Canfield, Phys. Rev. B **97**, 174517(R) (2018).

[41] U. S. Kaluarachchi, V. Taufour, A. E. Böhmer, M. A. Tanatar, S. L. Bud'ko, V. G. Kogan, R. Prozorov, and P. C. Canfield, Phys. Rev. B **93**, 064503 (2016).

[42] L. Xiang, U. S. Kaluarachchi, A. E. Böhmer, V. Taufour, M. A. Tanatar, R. Prozorov, S. L. Bud'ko, and P. C. Canfield, Phys. Rev. B **96**, 024511 (2017).

[43] V. Taufour, N. Foroozani, M. A. Tanatar, J. Lim, U. Kaluarachchi, S. K. Kim, Y. Liu, T. A. Lograsso, V. G. Kogan, R. Prozorov *et al.*, Phys. Rev. B **89**, 220509(R) (2014).

[44] V. G. Kogan and R. Prozorov, Phys. Rev. B **88**, 024503 (2013).

[45] M. Bristow, W. Knafo, P. Reiss, W. Meier, P. C. Canfield, S. J. Blundell, and A. I. Coldea, Phys. Rev. B **101**, 134502 (2020).

[46] Y.-B. Liu, Y. Liu, and G.-h. Cao, J. Phys.: Condens. Matter **34**, 093001 (2022).

[47] M. P. Smylie, K. Willa, J.-K. Bao, K. Ryan, Z. Islam, H. Claus, Y. Simsek, Z. Diao, A. Rydh, A. E. Koshelev *et al.*, Phys. Rev. B **98**, 104503 (2018).

[48] R. Khasanov, W. R. Meier, S. L. Bud'ko, H. Luetkens, P. C. Canfield, and A. Amato, Phys. Rev. B **99**, 140507(R) (2019).

[49] D. Torsello, G. A. Ummarino, J. Bekaert, L. Gozzelino, R. Gerbaldo, M. A. Tanatar, P. C. Canfield, R. Prozorov, and G. Ghigo, Phys. Rev. Appl. **13**, 064046 (2020).

[50] C.-R. Hu, Phys. Rev. B **6**, 1756 (1972).

[51] Y. J. Song, J. S. Ghim, J. H. Yoon, K. J. Lee, M. H. Jung, H.-S. Ji, J. H. Shim, Y. Bang, and Y. S. Kwon, Europhys. Lett. **94**, 57008 (2011).

[52] G. Blatter, M. V. Feigel'man, V. B. Geshkenbein, A. I. Larkin, and V. M. Vinokur, Rev. Mod. Phys. **66**, 1125 (1994).

[53] K. Cho, A. Fente, S. Teknowijoyo, M. A. Tanatar, K. R. Joshi, N. M. Nusran, T. Kong, W. R. Meier, U. Kaluarachchi, I. Guillamón *et al.*, Phys. Rev. B **95**, 100502(R) (2017).

[54] K. R. Joshi, N. M. Nusran, M. A. Tanatar, K. Cho, W. R. Meier, S. L. Bud'ko, P. C. Canfield, and R. Prozorov, Phys. Rev. Appl. **11**, 014035 (2019).

[55] V. G. Kogan, R. Prozorov, and V. Mishra, Phys. Rev. B **88**, 224508(R) (2013).

[56] S. V. Dordevic, D. N. Basov, and C. C. Homes, Sci. Rep. **3**, 1713 (2013).

[57] V. G. Kogan, Phys. Rev. B **87**, 220507(R) (2013).

[58] A. A. Abrikosov and L. P. Gor'kov, J. Exptl. Theoret. Phys. **39**, 1781 (1960) [Sov. Phys.-JETP 12, 1243 (1961)].

[59] A. N. Thaler, Structural and magnetic properties and superconductivity in $Ba(Fe_{1-x}TM_x)_2As_2$ (TM = Ru, Mn, Cr/Co, Mn/Co) single crystals, Ph.D. thesis, Iowa State University, Digital Repository, Ames, 2012, https://lib.dr.iastate.edu/etd/12970/.

[60] Y. Tomioka, M. Naito, and K. Kitazawa, Physica C **215**, 297 (1993).